minerals

MDPI

Article

Geochemical Characteristics of A-Type Granite near the Hongyan Cu-Polymetallic Deposit in the Eastern Hegenshan-Heihe Suture Zone, NE China: Implications for Petrogenesis, Mineralization and Tectonic Setting

Chen Mao [1], Xinbiao Lü [1,2,*] and Chao Chen [2]

[1] Faculty of Earth Resources, China University of Geosciences, Wuhan 430074, China; maochen_110@cug.edu.cn

[2] Institute of Geological Survey, China University of Geosciences, Wuhan 430074, China; chenchao_109@163.com

* Correspondence: luxb@cug.edu.cn; Tel.: +86-159-7293-4906

Received: 11 February 2019; Accepted: 16 April 2019; Published: 18 May 2019

Abstract: In the eastern Hegenshan-Heihe suture zone (HHSZ) of NE China, Cu-Au hydrothermal mineralization at the newly discovered Hongyan deposit is associated with the Shanshenfu alkali-feldspar granite (SAFG). Zircon U-Pb dating showed that the inner phase and outer phase of the SAFG were formed at 298.8 ± 1.0 Ma and 298.5 ± 1.0 Ma, respectively. Whole rock geochemistry suggests that the SAFG can be classified as an A-type granite. Halfnium isotopes and trace elements in zircon suggest that the SAFG has high Ti-in-zircon crystallization temperature (721–990 °C), high magmatic oxygen fugacity and largely positive $\varepsilon_{Hf}(t)$ (from +6.0 to +9.9). We proposed that the SAFG was derived from crustal assimilation and fractional crystallization of juvenile crust metasomatized by subducting oceanic crust. The high oxygen fugacity of the SAFG suggests the chalcophile elements (e.g., Cu, Au) remained in the magma as opposed to the magma source. An arc-related juvenile source favors enrichment of Cu and Au in the resulting magma. Combined, these magmatic characteristics suggest Cu ± Au exploration potential for magmatic-hydrothermal mineralization related to the SAFG, and similar bodies along the HHSZ. The results obtained combined with regional geological background suggest that the Permian A-type granites and related mineralization along the HHSZ were formed in a post-collisional slab break-off process.

Keywords: Hegenshan-Heihe suture zone; Cu-Au hydrothermal mineralization; Hongyan deposit; Permian A-type granite; granite petrogenesis; magmatic oxygen fugacity; post-collisional slab break-off

1. Introduction

Since the introduction of the A-type granite classification by Loiselle and Wones [1], rocks of this type have been studied extensively due to their important geodynamic significance, complicated petrogenesis and economic potential [2–13]. It has been recognized that A-type granites can be formed in a variety of extensional regimes, such as continental back-arc extension, post-collisional extension or within-plate settings [2,14]. In recent years, there have been many studies on the origin and oxidation state of A-type granites and their relationships to mineralization [7–10,12,13]. In general, previous workers have related oxygen fugacity and a degree of magma contamination to different types of mineralization [7–10]. High magmatic oxygen fugacity and juvenile magma sources such as mantle-derived crust or partial melting of an oceanic slab have been related to Cu-Mo-Au-Pb-Zn

mineralization [7,8,10]. Low magmatic oxygen fugacity, and wall-rock interaction or assimilation of continental crust are associated with W-Sn mineralization [7–9]. The oxidation state and petrogenesis of A-type granites has important geological significance, not only for regional tectonic evolution, but also for understanding the metallogenic process related to A-type granites. Decoding this petrogenetic intricacy, inherent geodynamic background and the related metallogenic process requires the use of an integrated whole rock geochemical and zircon chemical approach. Zircon chemistry relates to crystallization temperature and oxygen fugacity (fo_2) of magma [15–18], the composition of parental melts [19,20], source-rock type and crystallization environment [21–23]. The refractory nature and low elemental diffusion [24] mean that zircon chemistry remains unchanged through most geological processes, such as hydrothermal alteration, providing a powerful tool for documenting magmatic conditions (e.g., magma source and fo_2) and the resulting behavior of elements such as Cu [25–28].

In northeastern China (NE China), numerous Permian A-type granitoids (260–300 Ma) have been identified along the Hegenshan-Heihe suture zone (HHSZ) in the past two decades (Figure 1a,b) [3,4,29–32]. These A-type granites are on the eastern side of the larger Central Asian Orogenic Belt (CAOB, Figure 1a). Previous studies have provided mineralogical and geochemical constraints on the types (A2 type), sources (crust-mantle mixing or crustal sources) and tectonic settings (post-orogenic extension or post-collisional extension) of the Permian A-type granites along the HHSZ [3,4,29–32]. Newly discovered hydrothermal deposits are associated with these Permian A-type granites, including Aoyoute Cu-polymetallic deposit (287 Ma), Bayandulan Cu-polymetallic deposit (284 Ma) and Ataiwula Cu-polymetallic deposit (276 Ma) [32]. Despite a clear relationship between Permian A-type granitoids and mineralization, there is debate about the petrogenesis and tectonic setting of these rocks, and influence of the magma source and magmatic oxygen fugacity on the related metallogenic process needs further research. The newly discovered Hongyan Cu-polymetallic deposit is located in the northeastern part of the HHSZ (Figure 1c), and contains Cu-polymetallic hydrothermal mineralization clearly associated with a Permian A-type granitoid. The deposit and surrounding rocks provide a good opportunity to study the petrogenesis and tectonic setting of Permian A-type granitoids and their possible relationship with hydrothermal mineralization.

In this paper, we present zircon U-Pb ages, trace elements data and Hf isotope data with whole rock major and trace element data from Permian A-type granite in the Hongyan Cu-polymetallic deposit. We then use these data to discuss the oxidation state, petrogenesis and tectonic setting of these rocks. The results provide new insights into the petrogenesis and tectonic setting of Permian A-type granites along the HHSZ, and highlight the exploration potential of these rocks.

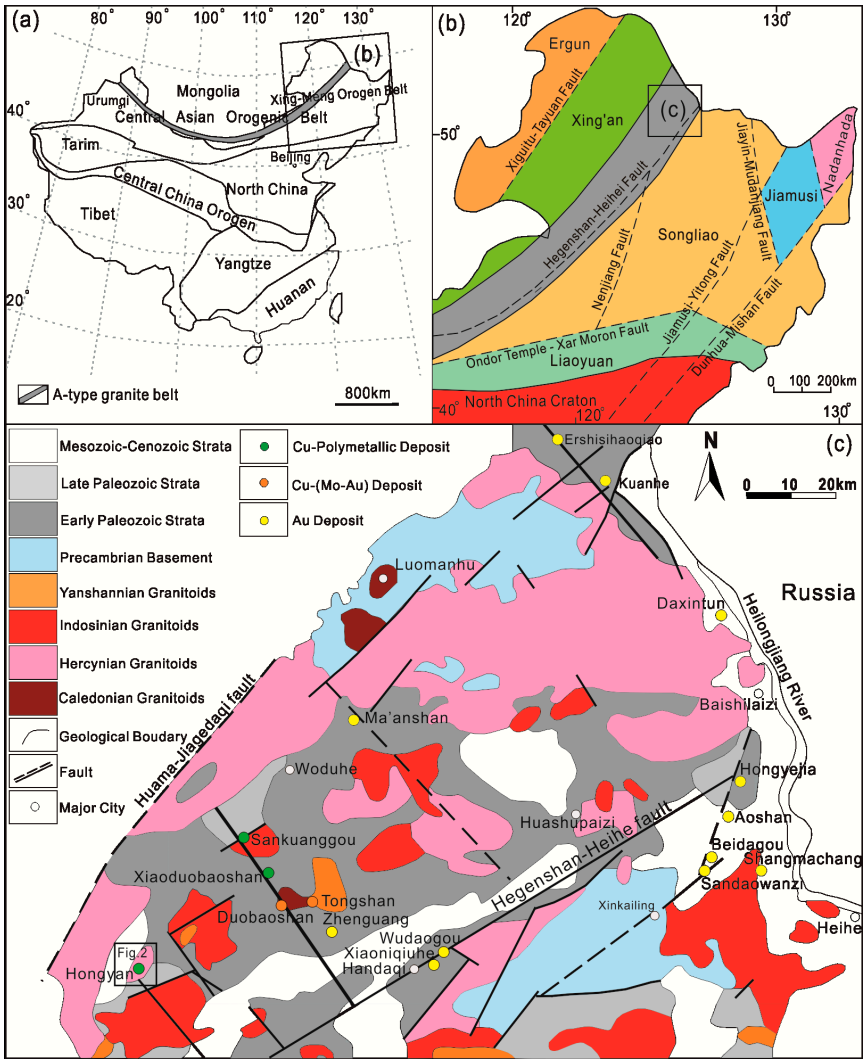

Figure 1. (**a**) Geotectonic division of China (after Mao et al. [33]); (**b**) tectonic subdivisions of northeast China (after Wu et al. [34]); (**c**) regional geological map of the northern Xing'an Block (after Gao et al. [35]).

2. Regional Geology

The Xing-Meng Orogen Belt (XMOB) is located in the eastern part of the CAOB, and was formed in the Permian through the collision between the Siberia block and North China block (Figure 1a) [34,36,37]. The XMOB is further subdivided by several NE-striking faults into different microcontinental massifs or terranes, including the Ergun massif, the Xing'an terrane, the Songliao terrane, the Jiamusi terrane and the Liaoyuan terrane (Figure 1b). These terranes have undergone EW-trending tectonic evolution of the Paleo-Asian Ocean during the Paleozoic and NNE-trending tectonic evolution of the western Pacific Ocean during the Mesozoic and Cenozoic.

The HHSZ is a suture zone resulting from the collision of the Xing'an and Songliao terranes (Figure 1b). The outcropping strata in the northern Xing'an terrane and its adjacent area can be approximately divided into four units (Figure 1c) [38,39]: (1) Sporadic distribution of Precambrian crystalline basement rocks composed of granulites, gneisses and schists; (2) extensive exposure of early Paleozoic metamorphosed volcanic and sedimentary rocks consisting of schist, sandy slate, marble and andesite, which are formed in continental margin and arc accretion settings; (3) the late Paleozoic units are similar to the early Paleozoic units but with lower metamorphic grades, such as the extensive distribution of the Baoligaomiao volcanic succession that represents Carboniferous subduction-related, mature, continental arc volcanism [40]; and (4) Mesozoic continental intermediate-felsic volcanic and sedimentary rocks, and Cenozoic sedimentary basin strata. Intense magmatic activity occurred along the HHSZ, which can be divided into the Caledonian, Hercynian, Indosinian and Yanshanian periods [41]. The Caledonian granitoids, consisting of granodiorite and quartz diorite, are sporadically distributed in the Luomahu and Duobaoshan areas. The Hercynian granitoids including granodiorite, monzogranite and alkali-feldspar granite are widely distributed on the northern side of the HHSZ. The Indosinian granitoids, consisting of monzogranite, syenogranite and two-mica granite, are widely distributed on both sides of the HHSZ. The Yanshanian granitoids, being composed of quartz diorite, granodiorite, tonalite and biotite granite, exhibit a sporadic distribution (Figure 1c) [4,42].

Intense hydrothermal activity was associated with these periods of magmatism, and resulted in various types of hydrothermal deposits, primarily including skarn Cu-polymetallic deposits (e.g., Sankuanggou and Xiaoduobaoshan), porphyry Cu-(Mo-Au) deposits (e.g., Duobaoshan and Tongshan) and epithermal Au deposits (e.g., Shangmachang, Beidagou, Sandaowanzi, Tianwangtaishan and Zhenguang, Figure 1c) [34,43,44], which constitute the northeastern segment of the Xing'an Cu-Mo-Fe-Pb-Zn-Au belt [37,45]. These deposits are located in a nearly NE-trending band along the HHSZ and its secondary NE- and NW-trending faults (Figure 1c).

3. Deposit Geology

The Hongyan Cu-polymetallic deposit comprises three orebodies (from E125°01′28″ to E125°06′30″, from N49°33′30″ to N49°42′30″; Figure 2), located in the northeastern part of the HHSZ (Figure 1c). Paleozoic and Mesozoic volcanic rocks are widespread near the deposit (Figure 2). Paleozoic volcanic rocks mainly include the Upper Carboniferous–Lower Permian Baoligaomiao Formation, which is a suite of continental volcanic rocks composed of rhyolitic tuff, andesitic tuff and basalt [46]. Mesozoic volcanic rocks are subdivided into the Lower Jurassic Manitu Formation, the Upper Cretaceous Baiyingaolao Formation and Damoguaihe Formation. The Manitu Formation comprises dacitic ignimbrite and dacite. The Baiyingaolao Formation is mainly composed of rhyolite, rhyolitic volcanic breccias and rhyolitic ignimbrite. The Damoguaihe Formation is mainly composed of conglomerate, fine sandstone and tuff breccias [46]. Steeply dipping brittle faults are dominantly NE-trending (e.g., F1 and F2), NWW-trending (e.g., F3, F4, F5, F6, F7 and F9) and E-trending faults (e.g., F8). The Shanshenfu alkali-feldspar granite (SAFG) with an exposed area of ~75 km^2 dominates plutonic rocks. The SAFG intrudes Paleozoic volcanic rocks with an irregular contact and is covered by Mesozoic volcanic rocks and Quaternary sediments (Figure 2).

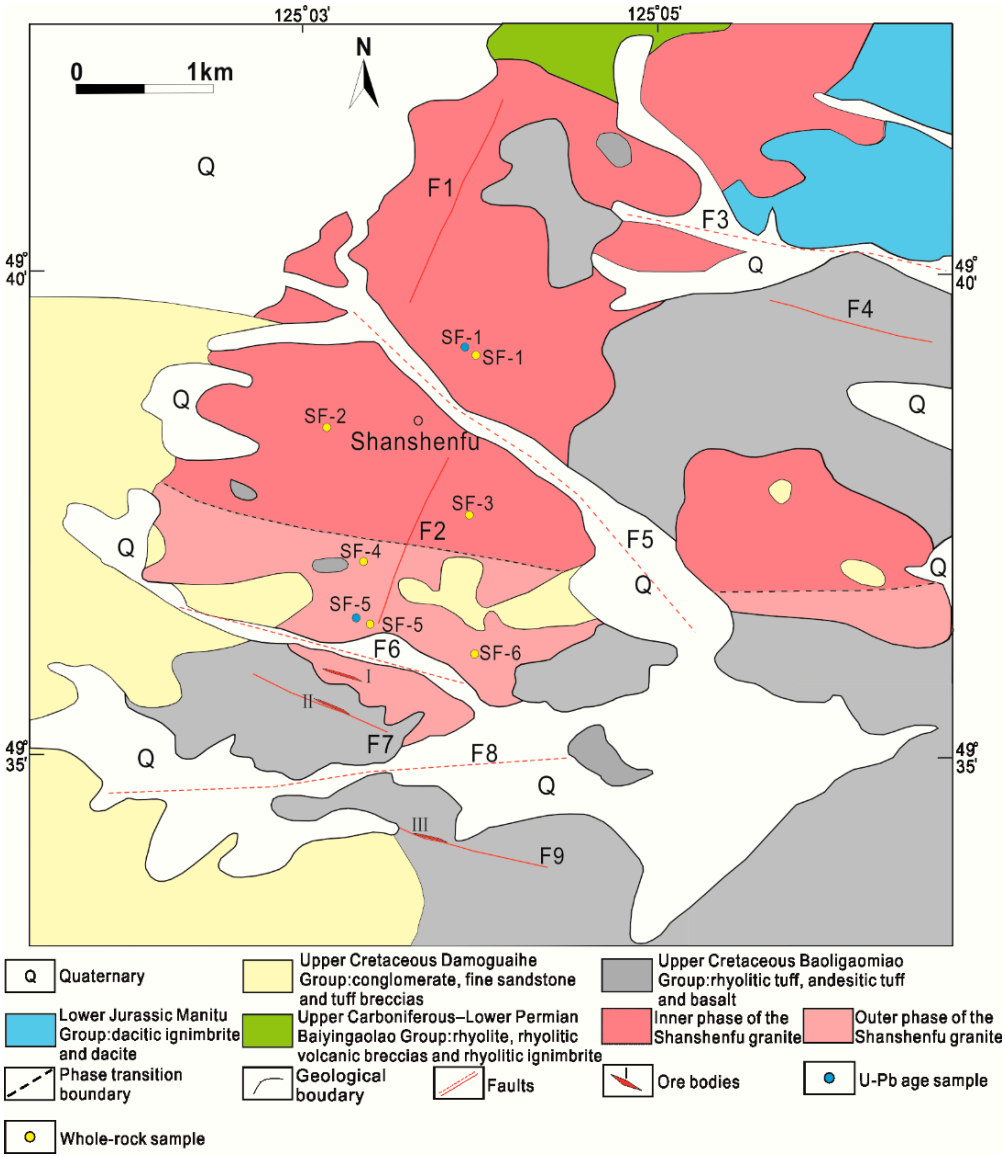

Figure 2. Geological sketch of the Hongyan Cu-polymetallic deposit [46].

The SAFG comprises an inner medium-grained phase and outer fine-grained phase (Figure 2). The boundary between the phases is gradational. The inner phase contains subhedral perthite (50%–55%), anhedral quartz (30%–35%), plagioclase (5%–10%), hornblende (0%–5%) and muscovite (0%–5%, Figures 3a and 4a). The outer phase comprises subhedral perthite (55%–60%), anhedral quartz (25%–30%), plagioclase (5%–10%), hornblende (0%–5%) and muscovite (0%–5%, Figures 3b and 4b). Accessory minerals are magnetite (Figure 4d), zircon and apatite.

The SAFG is pervasively altered by potassic (Figure 3c) and quartz-sericite alteration (Figure 4c), and is accompanied by some disseminated Cu mineralization (Figure 4d). Cu-polymetallic mineralization generally occurs as quartz veins and veinlets in the SAFG and the Baoligaomiao Formation, which is structurally controlled by tensile cracks and NWW-striking faults, respectively (Figure 2). Three vein-shaped mineralized bodies are identified in the Hongyan Cu-polymetallic deposit, which from north to south are No. I, II and III, respectively [46] (Figure 2): The No. I ore body hosted in the outer phase of the SAFG develops NWW-trending ore veins with a length of 250 m, an average thickness of 3.1 m and Cu grades of 0.5%–1.5%; the No. II ore body hosted in the Baoligaomiao Formation develops NWW-trending and N-dipping ore veins with a length of 220 m, an average thickness of 2.3 m and Cu, Au and Ag grades of 0.4%–1.2%, 0.34–2.21 g/t and 0.76–21.6 g/t, respectively; the No. III ore body hosted in the Baoligaomiao Formation develops NWW-trending and N-dipping ore veins with a length of 215 m, an average thickness of 1.8 m and Cu, Au and Ag grades of 0.5%–1.35%, 0.27–2.62 g/t and 0.64–16.2 g/t, respectively.

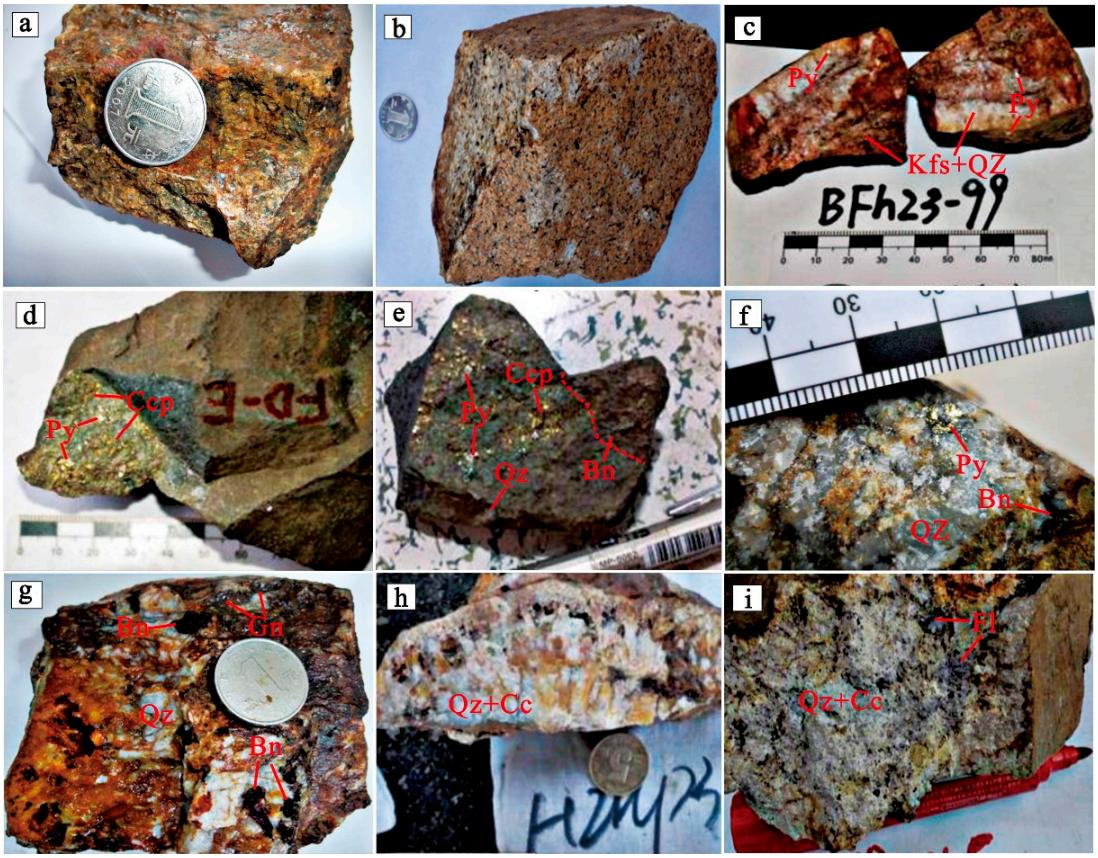

Figure 3. Hand specimen photos of the Shanshenfu alkali-feldspar granite and Stage I–III mineralization from the Hongyan Cu-polymetallic deposit. (**a**) Medium-grained alkali-feldspar granite (inner phase); (**b**) fine-grained alkali-feldspar granite (outer phase); (**c**) Stage I K-feldspar–quartz–pyrite vein; (**d**) Stage II disseminated chalcopyrite–pyrite–quartz mineralization; (**e**) Stage II quartz–pyrite–chalcopyrite–bornite vein; (**f**) Stage II quartz–pyrite–bornite vein; (**g**) Stage II quartz–bornite–galena vein; (**h**) Stage III quartz–calcite vein; (**i**) Stage III quartz–calcite–fluorite vein. Qz—quartz, Kf—K-feldspar, Py—pyrite, Ccp—chalcopyrite, Bn—bornite, Gn—galena, Cc—calcite, Fl—fluorite.

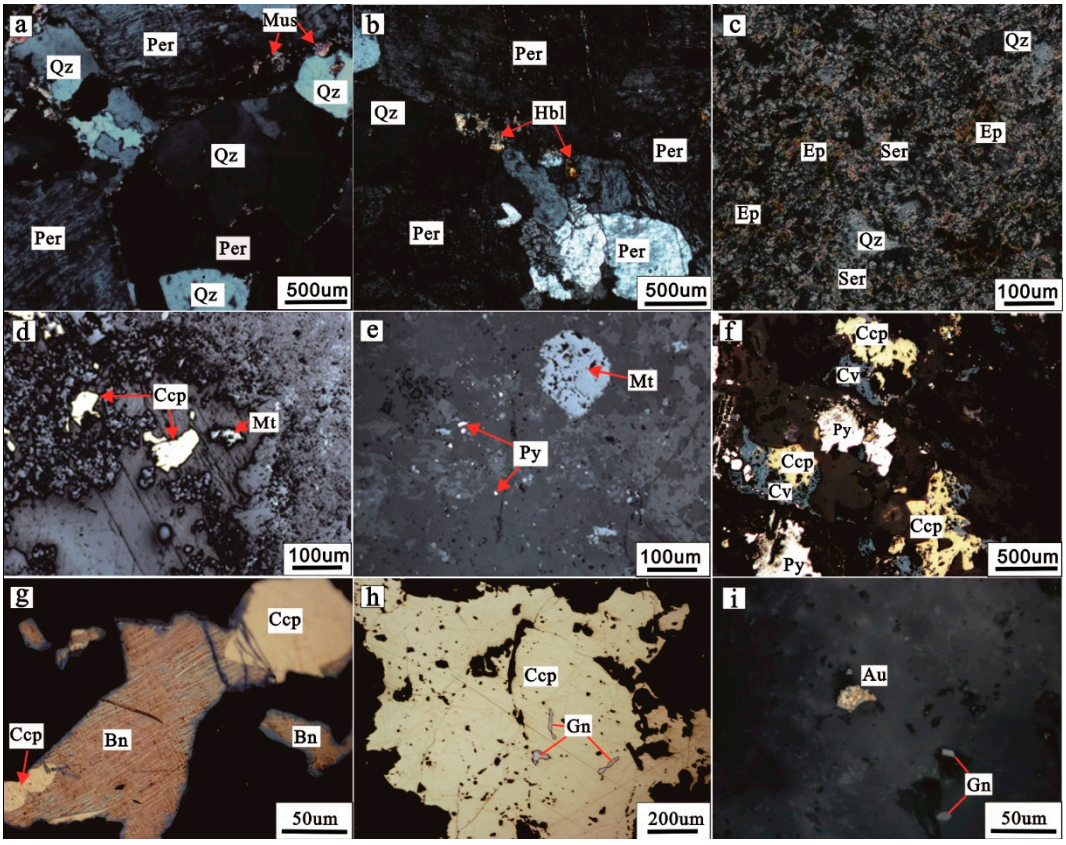

Figure 4. Transmitted light (**a**–**c**) and reflected light (**d**–**i**) microphotographs of the Shanshenfu alkali-feldspar granite, hydrothermal alteration features and metal mineral assemblages. (**a**) Medium-grained alkali-feldspar granite (inner phase); (**b**) fine-grained alkali-feldspar granite (outer phase); (**c**) widespread alteration of quartz, sericite and epidote in the granite; (**d**) chalcopyrite and magnetite in fine-grained alkali-feldspar granite (outer phase); (**e**) pyrite and magnetite in Stage I K-feldspar–quartz–pyrite vein; (**f**) chalcopyrite intergrown with pyrite replaced by the covellite in Stage II quartz vein; (**g**) chalcopyrite replace bornite in Stage II quartz vein; (**h**) chalcopyrite intergrown with galena in Stage II quartz vein; (**i**) visible gold intergrown with galena in Stage II quartz vein. Py—pyrite, Ccp—chalcopyrite, Bn—bornite, Gn—galena, Mt—magnetite, Cv—covellite, Au—native gold, Qz—quartz, Per—Perthite, Mus—Muscovite, Hbl—Hornblende, Ser—sericite, Ep—epidote.

4. Mineralization and Alteration in Ore Bodies

Based on our field and petrographic observations, the main ore minerals are chalcopyrite and pyrite, with minor bornite, covellite, galena, sphalerite, magnetite and native gold. The most common gangue minerals are quartz, K-feldspar, sericite, muscovite, chlorite, epidote, calcite and fluorite. Silicification is well developed and closely related to sulfide mineralization. Based on hydrothermal alteration mineral assemblages, we identify three stages of mineralization (Figure 5): Quartz ± K-feldspar ± pyrite (Stage I), quartz + chalcopyrite ± pyrite ± bornite ± sphalerite ± galena (Stage II) and quartz + carbonate ± fluorite (Stage III). Stage I is widely distributed in No. I and II ore bodies, which is defined by the occurrence of quartz and K-feldspar with minor pyrite and magnetite as veins (Figures 3c and 4e). Stage II is the main ore-forming stage and mainly distributed in the three ore bodies, which is represented by the widespread occurrence of quartz, chalcopyrite and pyrite minerals as veins or veinlets with minor bornite, covellite, galena and sphalerite (Figures 3d–g and 4f–h). Chalcopyrite replaces early bornite and is commonly intergrown with pyrite and galena (Figure 4g,h). Chalcopyrite and pyrite are partly replaced by covellite (Figure 4f). Gold mineralization is most commonly hosted within sulfide minerals in this stage, and visible gold can be found in the quartz veins (Figure 4i). Stage III is mainly distributed in No. II and III ore bodies, which is characterized by the appearance

of calcite and quartz with minor fluorite as veins or veinlets (Figure 3h–i). Small amounts of pyrite occur in quartz-calcite veins, and gold mineralization is less in this stage. The presence of fluorite mineralization has been reported to be closely related to A-type granites [47,48]. Combined, the development of Cu-polymetallic mineralization in the SAFG and widespread K-feldspar alteration and fluorite mineralization in ore bodies suggest that these ore-forming hydrothermal fluids are mainly derived from the SAFG.

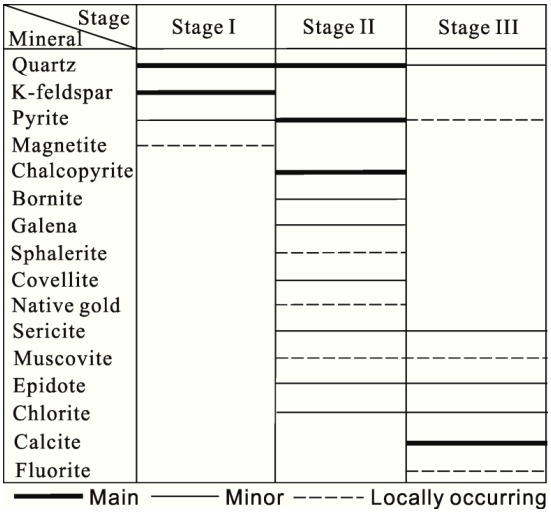

Figure 5. Paragenetic sequence for the Hongyan Cu-polymetallic deposit.

5. Analytical Methods

5.1. Zircon U-Pb Dating Analysis

The sample SF-1 from the inner phase and the sample SF-5 from the outer phase were collected for geochronology (Figure 2). Zircon grains were separated using conventional heavy liquid and magnetic techniques, and then handpicked under a binocular microscope. Handpicked zircon grains were mounted on adhesive tape, enclosed in epoxy resin and polished so that approximately half of each zircon is exposed. To study interior textures of zircons cathodoluminescence (CL) images were collected with a JEOL JXA-8100 electron microprobe (TESCAN MIRA 3 LMH FE-SEM, TESCAN, Brno, Czech Republic) at the State Key Laboratory of Geological Processes and Mineral Resources, China University of Geosciences, Wuhan. Zircon U-Th-Pb measurements were done under a 32 μm diameter laser beam at the same laboratory using a Geo-Las 2005 System. An Agilent 7500a ICP-MS (Agilent, Santa Clara, CA, USA) instrument was used to acquire ion-signal intensities with a 50 mJ/pulse 193 nm ArF-excimer laser at 10 Hz and a homogenizing, imaging optical system (MicroLas, Göttingen, Germany). The data acquisition for each analysis took 100 s (40 s on background and 60 s on signal). Detailed instrumentation and analytical accuracy description were given by Liu et al. [49,50]. Time-dependent drifts of U-Th-Pb isotopic ratios were corrected using a linear interpolation (with time) for every six analyses according to the variations of external standard zircon 91,500 (2 zircon 91,500 + 6 samples + 2 zircon 91,500) [50]. The ages are calculated by inhouse software ICPMSDataCal (version 6.9, China University of Geosciences) [49] and concordia diagrams were made by Isoplot/Ex ver3.0 [51]. Errors on individual analyses are quoted at the 1σ level, whereas errors on weighted mean ages are quoted at the 2σ (95% confidence) level. Trace element compositions of zircon are calibrated against GSE-1G combined with internal standardization ^{29}Si [50].

Zircon Ce and Eu anomalies, Ti-in-zircon temperatures and magmatic oxygen fugacity (fo_2) were calculated using the trace element compositions of zircons collected during the same analysis interval as U-Pb dating. The method for calculating these parameters has been described in Ferry and Watson [16] and Trail et al. [17,18]. CGDK software [52] was used for plotting data.

5.2. Zircon Lu-Hf Isotopes Analysis

In-situ zircon Hf isotopic analyses were conducted using a Neptune Plus MC-ICP-MS (Thermo Fisher Scientific, Germany) equipped with a Geolas 2005 excimer ArF laser ablation system (Lambda Physik, Göttingon, Germany) at the state Key Laboratory of Geological Processes and Mineral Resources, China University of Geosciences (Wuhan). All data were acquired on zircon in single spot ablation mode at a pulse rate of 20 Hz at 200 mJ with a spot size of 44 μm in this study. Each measurement consisted of 20 s of acquisition of the background signal followed by 50 s of ablation signal acquisition. Detailed operating conditions for the laser ablation system and the analytical method are the same as description by Hu et al. [53]. The $^{176}Hf/^{177}Hf$ ratios of the standard zircon (GJ1) were 0.282013 ± 0.000022 (2σ, n = 276), in agreement with recommended values within 2σ error [54,55]. Offline selection and integration of analyte signals, and mass bias calibrations were performed using ICPMSDataCal [50].

5.3. Whole-Rock Major and Trace Element Analyses

Three samples from the inner phase (from SF-1 to SF-3) and three samples from the outer phase (from SF-4 to SF-6) were collected for major and trace element determinations. All the samples are unaltered and unweathered. Geochemical analyses were carried out at the Guangzhou Institute of Geochemistry, Chinese Academy of Sciences (GIG-CAS). Major element oxides were analyzed using a Rigaku RIX 2000 X-ray fluorescence spectrometer (XRF, Panalytical, Almelo, The Netherlands), and analytical uncertainties are mostly between 1% and 5% [56]. Trace elements were obtained by inductively coupled plasma-mass spectrometry (ICP-MS, Perkin Elmer Elan 9000, Perkin, Waltham, MA, USA) after acid digestion of samples in high-pressure Teflon vessels, and detailed procedures are described by Li et al. [56]. The USGS and Chinese National standards AGV-2, GSR-1, GSR-2, MRG-1, BCR-1, W-2 and G-2 were chosen for calibrating element concentrations of the analyzed samples. Analytical precision of REE and other incompatible element analyses is typically 1%–5%.

6. Results

6.1. Zircon U-Pb Ages

The zircon U-Pb ages for 23 zircons are shown in Table 1. Most of the zircon grains from two samples (SF-1 and SF-5) are euhedral and prismatic, and are relatively transparent and colorless. They have a length between 61 μm and 179 μm, with length to width ratios between approximately 1:1–3:1 (Figure 6a,b). CL images show that most zircons have magmatic oscillatory overgrowth rims, although a few zircons with high uranium contents are dark brown and turbid (Figure 6a,b). Most zircons have high Th/U ratios >0.5, which are typical of an igneous origin. Twelve spot analyses of zircons from sample SF-1 yield $^{206}Pb/^{238}U$ ages of 297 Ma to 300 Ma (Figure 6c) with a weighted mean age of 298.8 ± 1.0 Ma (MSWD = 0.27) for all 12 analyses. Eleven spot analyses from sample SF-5 yield $^{206}Pb/^{238}U$ ages between 297 Ma and 300 Ma (Figure 6d) with a weighted mean age of 298.5 ± 1.0 Ma (MSWD = 0.36) for all 11 analyses. These ages are coeval and are interpreted as the crystallization age for the SAFG.

Table 1. Zircon LA-ICP-MS U-Pb data of the Shanshenfu alkali-feldspar granite.

Spot	Trace Elements (ppm)			Isotopic Ratio						Apparent Age (Ma)					
	U	Th	Th/U	$^{207}Pb/^{235}U$	1σ	$^{206}Pb/^{238}U$	1σ	$^{207}Pb/^{206}Pb$	1σ	$^{206}Pb/^{238}U$	1σ	$^{207}Pb/^{235}U$	1σ	$^{207}Pb/^{206}Pb$	1σ
Sample SF-1															
SF1-1	635	337	0.53	0.3362	0.0039	0.0472	0.0002	0.0517	0.0006	297	1.7	294	4.0	272	21.3
SF1-2	591	349	0.59	0.3425	0.0046	0.0475	0.0002	0.0523	0.0007	299	1.9	299	4.6	298	−2.8
SF1-3	817	683	0.84	0.3341	0.0035	0.0473	0.0002	0.0512	0.0005	298	1.8	293	3.8	250	24.1
SF1-4	656	345	0.53	0.3413	0.0046	0.0475	0.0001	0.0521	0.0007	299	1.6	298	4.6	300	31.5
SF1-5	1413	809	0.57	0.3434	0.0024	0.0473	0.0001	0.0526	0.0004	298	1.6	300	3.0	322	14.8
SF1-6	495	262	0.53	0.3403	0.0052	0.0475	0.0002	0.0519	0.0008	299	1.8	297	5.1	283	30.6
SF1-7	1130	738	0.65	0.3468	0.0029	0.0476	0.0002	0.0528	0.0004	300	2.0	302	3.4	320	16.7
SF1-8	988	482	0.49	0.3463	0.0031	0.0476	0.0002	0.0528	0.0005	300	1.8	302	3.5	320	20.4
SF1-9	822	430	0.52	0.3465	0.0033	0.0476	0.0002	0.0528	0.0005	300	1.9	302	3.7	320	20.4
SF1-10	1202	673	0.56	0.3418	0.0024	0.0475	0.0002	0.0522	0.0004	299	2.0	299	3.0	295	14.8
SF1-11	191	144	0.76	0.3417	0.0124	0.0473	0.0002	0.0523	0.0019	298	2.0	298	11.1	298	79.6
SF1-12	719	283	0.39	0.3428	0.0046	0.0475	0.0002	0.0523	0.0007	299	1.8	299	4.6	298	−2.8
Sample SF-5															
SF5-1	613	326	0.53	0.3459	0.0037	0.0476	0.0002	0.0527	0.0005	300	1.9	302	3.9	317	22.2
SF5-2	215	148	0.69	0.3457	0.0103	0.0475	0.0002	0.0527	0.0015	299	1.8	302	9.2	317	69.4
SF5-3	698	481	0.69	0.3456	0.0044	0.0475	0.0002	0.0528	0.0006	299	2.0	301	4.4	320	25.9
SF5-4	680	214	0.31	0.3413	0.004	0.0473	0.0001	0.0524	0.0006	298	1.6	298	4.1	302	25.9
SF5-5	1062	490	0.46	0.3397	0.0027	0.0475	0.0002	0.0519	0.0004	299	1.7	297	3.2	280	18.5
SF5-6	239	144	0.6	0.3451	0.0087	0.0475	0.0002	0.0526	0.0013	299	1.8	301	7.9	309	55.6
SF5-7	1077	67	0.06	0.3433	0.0025	0.0472	0.0001	0.0527	0.0004	298	1.6	300	3.1	317	23.1
SF5-8	201	95	0.47	0.3472	0.0142	0.0476	0.0001	0.0531	0.0022	300	1.7	303	12.5	332	92.6
SF5-9	1407	651	0.46	0.3501	0.0024	0.0472	0.0001	0.0538	0.0003	297	1.6	305	3.1	365	13.0
SF5-10	583	243	0.42	0.3407	0.0058	0.0472	0.0001	0.0523	0.0009	297	1.7	298	5.5	298	41.7
SF5-11	1213	646	0.53	0.3422	0.0027	0.0473	0.0001	0.0525	0.0004	298	1.6	299	3.2	306	12.0

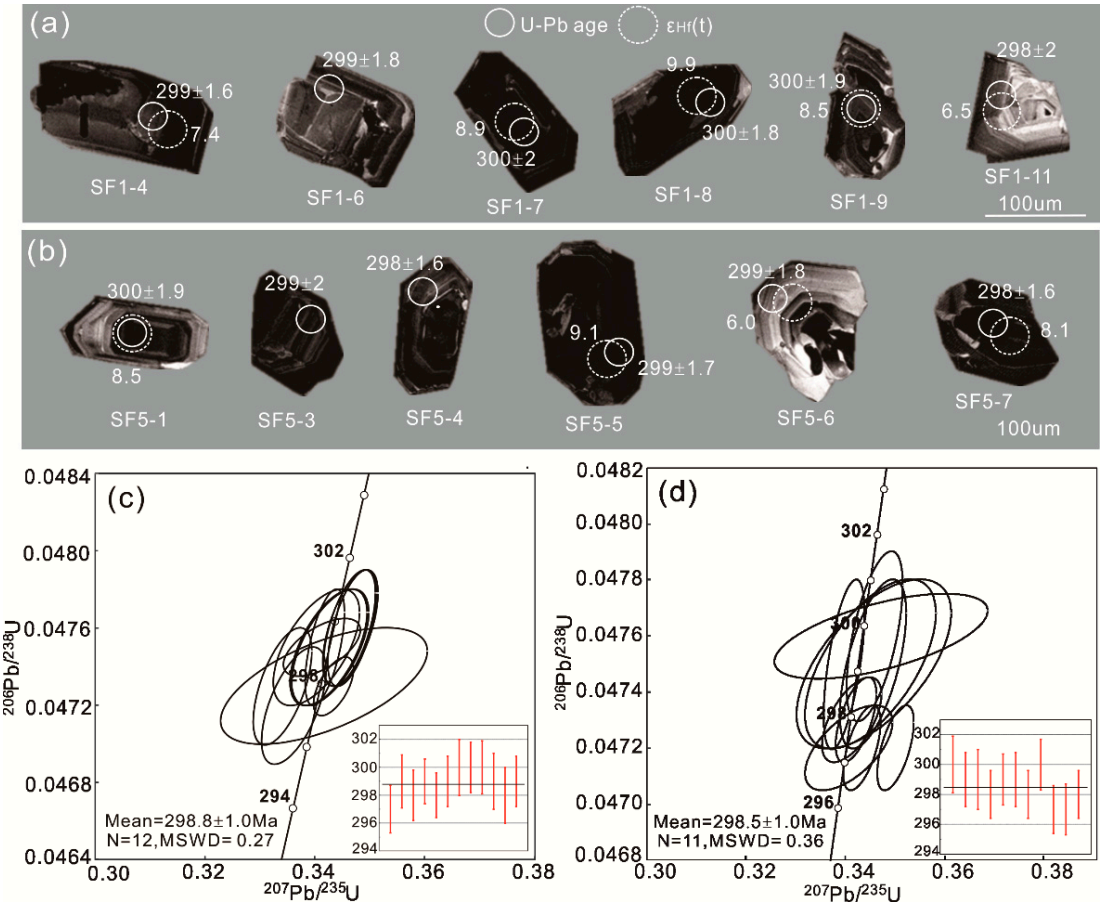

Figure 6. Zircon cathodoluminescence (CL) images and zircon U-Pb concordant curves for SF-1 from the inner phase (**a**,**c**) and SF-5 from the outer phase (**b**,**d**) of the Shanshenfu alkali-feldspar granite.

6.2. Zircon Trace Element, Ti-in-Zircon Temperature and Oxygen Fugacity

Trace element compositions of zircons are listed in Table 2, and the corresponding chondrite-normalized REE patterns are plotted in Figure 7. The zircons of sample SF-1 and SF-5 have ΣREE contents ranging from 3815 ppm to 10,727 ppm and 1411 ppm to 8447 ppm, respectively, Ce anomalies ranging from 1.2 to 276 (average of 86) and from 1.7 to 215 (average of 44), respectively, Eu anomalies ranging from 0.01 to 0.09 and from 0 to 0.38, respectively and Ti contents ranging from 8.6 ppm to 58.3 ppm and from 4.8 ppm to 173 ppm, respectively. Typical igneous zircon has Ti values ≤75 ppm [21]. One grain in our study has high Ti value (SF5-9 = 173 ppm). A value this high is unusual for igneous zircon and may be the result of inclusions (e.g., ilmenite) in the analysis; this analysis is excluded from the following discussion. The temperature of the melt during zircon crystallization was calculated by the Ti-in-zircon thermometer [16] as shown in the following Equation (1):

$$T_{zircon}\left(^{\circ}\mathrm{C}\right) = 4800/\left(5.711 - \lg\left(Ti_{zircon}\right) - \lg\left(Si_a\right) + \lg\left(Ti_a\right)\right) - 273 \quad (1)$$

As quartz is one of the major mineral phases in the SAFG, the activity of silica (Si_a) is set to 1. Due to the absence of rutile in the SAFG, the activity of titanium (Ti_a) is conservatively estimated to be 0.6 [15,57]. The calculated Ti-in-zircon temperatures for the inner phase (sample SF-1) and the outer phase (sample SF-5) are in the range of 773 °C to 990 °C (average of 854 °C) and 721–919 °C (average of 841 °C, Table 2), respectively. A new calibration has been presented by Trail et al. [17,18] to determine

the oxygen fugacity of magmatic melt based on the incorporation of cerium into zircon and Ti-in-zircon temperature, which can be expressed by the following empirical equation:

$$\ln\left(\frac{\mathrm{Ce}}{\mathrm{Ce}^*}\right)_D = (0.1156 \pm 0.0050) \times \ln(f_{o2}) + \frac{13860 \pm 708}{T(\mathrm{K})} - 6.125 \pm 0.484 \quad (2)$$

where fo_2 represents oxygen fugacity, and T is absolute temperature calculated by revised Ti-in-zircon thermometry. The Ce anomaly can be estimated by the following equation:

$$\left(\frac{\mathrm{Ce}}{\mathrm{Ce}^*}\right)_D \approx \left(\frac{\mathrm{Ce}}{\mathrm{Ce}^*}\right)_{\mathrm{CHUR}} = \frac{\mathrm{Ce_N}}{\sqrt{\mathrm{La_N} \cdot Pr_N}} \quad (3)$$

where $\mathrm{Ce_N}$, $\mathrm{La_N}$ and $\mathrm{Pr_N}$ are chondrite-normalized values for Ce, La and Pr in zircon, respectively.

The $\lg(fo_2)$ values for the zircons of the inner phase and the outer phase are in the range of −21.3 to −3.4 (average of −10.3) and from −24.2 to −2.7 (average of −13.1), respectively, with corresponding ΔFMQ values of −8.4 to +10.6 (average of +3.1) and from −9.4 to +10.6 (average of +0.7), respectively (Table 2).

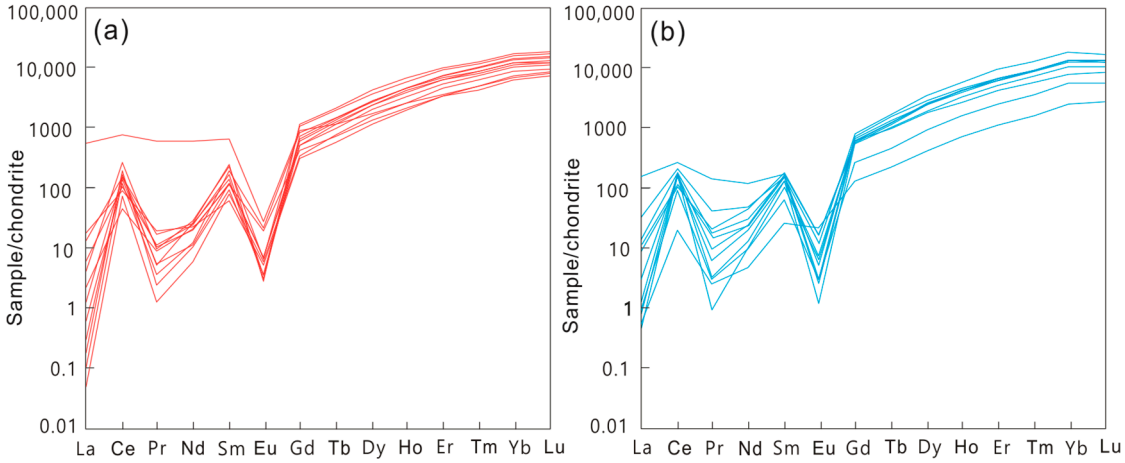

Figure 7. Chondrite-normalized REE patterns for the zircons from the Shanshenfu alkali-feldspar granite. (**a**) SF-1 (inner phase); (**b**) SF-5 (outer phase). Normalization values for chondrite are from McDonough and Sun [58].

6.3. Zircon Lu–Hf Isotopes

The analytical results on Hf isotopes for zircons are listed in Table 3. The $\varepsilon_{Hf}(t)$ values are calculated using their U-Pb ages. Seven spots from the inner phase show a range of initial $^{176}Hf/^{177}Hf$ ratios from 0.282955 to 0.283052 and $\varepsilon_{Hf}(t)$ values from +6.5 to +9.9, with the two-stage Hf model ages (T_{DM2}) from 394 Ma to 587 Ma. Nine spots from the outer phase show a range of initial $^{176}Hf/^{177}Hf$ ratios from 0.282941 to 0.283029 and $\varepsilon_{Hf}(t)$ values from +6.0 to +9.1, with T_{DM2} from 441 Ma to 614 Ma.

Table 2. Zircon trace element abundance, Ce and Eu anomalies, Ti-in-zircon temperatures (T) and magmatic oxygen fugacity (fO_2) of the Shanshenfu alkali-feldspar granite.

Spot	La	Ce	Pr	Nd	Sm	Eu	Gd	Tb	Dy	Ho	Er	Tm	Yb	Lu	ΣREE	Ti	δCe	δEu	T_{Ti}	lg(fO_2)	FMQ Buffer	△FMQ
	ppm	ppm	ppm	ppm	ppm	ppm	ppm	ppm	ppm	ppm	ppm	ppm	ppm	ppm	ppm	ppm			°C			
Sample SF-1																						
SF1-1	1.57	268	1.39	21.3	53.9	0.6	333	119	1451	510	2244	417	3937	663	10,019	16.3	39.2	0.01	837	−10.1	−13.7	3.6
SF1-2	2.23	103	1.63	18.4	39.1	0.32	224	82.2	1050	395	1808	346	3297	566	7931	33.2	11.7	0.01	917	−11.5	−12.2	0.7
SF1-3	0.88	44.6	1.23	15.5	27.3	1.78	135	43.3	506	182	829	159	1586	284	3815	58.3	9.3	0.09	990	−9.9	−11.1	1.2
SF1-4	6.60	92.0	2.77	15.9	15.0	0.47	95.2	33.9	450	176	854	172	1798	321	4026	22.6	4.7	0.04	872	−16.7	−13.1	−3.6
SF1-5	0.11	161	0.74	19.8	58.6	0.26	348	126	1590	570	2490	457	4227	679	10,727	19.1	120.8	0.01	854	−5.2	−13.4	8.2
SF1-6	210	750	84.6	433	154	2.44	280	67.4	674	217	934	179	1774	312	5861	24.6	1.2	0.04	882	−21.3	−12.9	−8.4
SF1-7	0.24	116	0.5	9.2	44.4	1.84	251	86.8	1097	385	1700	316	2933	475	7416	19.2	73.2	0.05	855	−7.0	−13.4	6.4
SF1-8	0.04	137	0.75	7.9	27.8	0.59	186	70.9	947	350	1602	306	2990	504	7130	8.6	174.8	0.03	773	−7.4	−15.1	7.7
SF1-9	0.49	152	1.45	14.3	27.2	0.61	163	59.1	757	281	1317	261	2633	443	6110	9.3	39.0	0.03	781	−12.6	−14.9	2.3
SF1-10	0.07	191	0.34	7.6	21.2	0.33	162	67.4	904	338	1576	297	2838	452	6855	13.9	270.5	0.02	820	−3.6	−14.1	10.5
SF1-11	5.14	147	2.31	18.6	33.7	0.28	208	81.2	1073	406	1859	362	3546	585	8322	16.7	9.2	0.01	840	−15.4	−13.7	−1.7
SF1-12	0.02	72.7	0.17	4.3	17.9	0.53	110	43.5	589	229	1105	224	2242	367	5005	14.2	276.0	0.04	823	−3.4	−14.0	10.6
Sample SF-5																						
SF5-1	3.49	99.6	2.87	32.7	42.1	1.53	198	60.2	707	237	1038	204	1995	334	4952	33.6	6.8	0.05	919	−13.5	−12.2	−1.3
SF5-2	0.50	184	0.49	9.6	30.9	0.11	180	69.9	936	358	1607	321	3265	500	7462	32.5	80.7	0.00	915	−4.3	−12.3	8.0
SF5-3	12.2	212	6.04	35.3	36.1	0.24	199	75.3	987	369	1676	336	3362	528	7822	12.1	5.3	0.01	807	−18.9	−14.4	−4.5
SF5-4	5.38	183	2.59	22.3	36.9	0.49	232	92.7	1142	382	1685	338	3349	488	7954	9.2	10.6	0.02	780	−17.6	−14.9	−2.7
SF5-5	0.16	135	0.11	6.7	20.7	0.51	168	63.6	876	320	1488	290	2977	431	6777	20.4	215.0	0.03	861	−2.7	−13.3	10.6
SF5-6	0.31	161	1.34	17.9	38.1	0.27	216	76.6	962	347	1561	320	3247	502	7450	18.9	53.8	0.01	853	−8.3	−13.4	5.1
SF5-7	57.0	260	19.2	84.4	38.8	1.45	171	57.9	748	271	1258	255	2667	409	6241	9.8	1.7	0.05	786	−24.2	−14.8	−9.4
SF5-8	1.14	156	0.83	13.9	30.1	0.69	188	74.1	970	357	1595	324	3276	473	7459	18.4	34.8	0.03	850	−10.0	−13.5	3.5
SF5-9	0.36	87.4	0.42	6.8	15.1	0.27	82.6	27.8	370	134	627	135	1424	225	3135	173	48.3	0.02	1158	-	-	-
SF5-10	0.20	20.0	0.35	3.4	6.19	1.98	42.1	13.2	160	60.9	285	59.2	651	107	1410	33.5	16.4	0.38	918	−10.2	−12.2	2.0
SF5-11	4.03	109	1.65	14.6	30.1	0.78	204	78.5	1068	403	1890	376	3683	585	8444	4.8	9.2	0.03	721	−21.0	−16.3	−4.7

Note: T_{Ti} (°C) is the Ti temperature of zircon, $\delta Ce = Ce_N/(La_N \times Pr_N)^{0.5}$, $\delta Eu = Eu_N/(Sm_N \times Gd_N)^{0.5}$; FMQ buffer is the buffer of the fayalite-magnetite-quartz, which is calculated using the formula FMQ buffer = −24,441.9/(T + 273) + 8.290 (±0.167) [59]; △FMQ = lgfO_2 − FMQ buffer.

Table 3. LA-MC-ICP-MS zircon Lu-Hf isotope data for the Shanshenfu alkali-feldspar granite.

Spot	$^{176}Hf/^{177}Hf$ [a]	1σ	$^{176}Lu/^{177}Hf$ [a]	1σ	$^{176}Yb/^{177}Hf$ [a]	1σ	Age (Ma)	ε_{Hf} (t) [b]	1σ	T_{DM1} (Ma) [c]	T_{DM2} (Ma) [d]	$f_{Lu/Hf}$
Sample SF-1												
SF1-1	0.282995	0.000015	0.002996	0.000008	0.086319	0.000235	297	7.9	0.74	384	507	−0.91
SF1-4	0.282982	0.000014	0.002209	0.000051	0.061855	0.001585	299	7.4	0.70	395	533	−0.93
SF1-7	0.283024	0.000015	0.004243	0.000064	0.115732	0.00164	300	8.9	0.75	353	450	−0.87
SF1-8	0.283052	0.000016	0.003983	0.000026	0.117902	0.00081	300	9.9	0.76	307	394	−0.88
SF1-9	0.283011	0.000014	0.003086	0.000051	0.089502	0.001556	300	8.4	0.72	362	476	−0.91
SF1-11	0.282955	0.000013	0.00128	0.000005	0.032593	0.000132	298	6.5	0.70	424	587	−0.96
SF1-12	0.282967	0.000014	0.002444	0.000009	0.068065	0.000324	299	6.9	0.73	420	563	−0.93
Sample SF-5												
SF5-1	0.283011	0.000017	0.004065	0.000056	0.11864	0.001618	300	8.4	0.79	372	476	−0.88
SF5-2	0.283020	0.000014	0.002091	0.000018	0.055445	0.0004	299	8.8	0.72	338	458	−0.94
SF5-5	0.283029	0.000017	0.003066	0.000016	0.090641	0.000562	299	9.1	0.79	335	441	−0.91
SF5-6	0.282941	0.000014	0.000794	0.000014	0.020234	0.000404	299	6.0	0.70	438	614	−0.98
SF5-7	0.283002	0.000014	0.003232	0.000016	0.093923	0.000628	298	8.1	0.72	377	494	−0.90
SF5-8	0.282948	0.000015	0.001153	0.000078	0.029802	0.002258	300	6.2	0.73	433	602	−0.97
SF5-9	0.283015	0.000014	0.003446	0.00001	0.099972	0.000247	297	8.6	0.72	359	468	−0.90
SF5-10	0.283025	0.000014	0.002295	0.000037	0.066671	0.001076	297	8.9	0.72	333	448	−0.93
SF5-11	0.283028	0.000015	0.003929	0.00002	0.113707	0.000769	298	9.0	0.75	344	443	−0.88

[a] The measured values; [b] Initial $^{176}Hf/^{177}Hf$ ratios were calculated using the measured $^{176}Lu/^{177}Hf$ ratios and the ^{176}Lu decay constant of 1.867×10^{-11} $year^{-1}$ [60], and ε_{Hf} values were calculated using the chondritic ratios of $^{176}Hf/^{177}Hf$ (=0.282772) and $^{176}Lu/^{177}Hf$ (=0.0332) [61]; [c] The single-stage model age (T_{DM1}) was calculated using the present-day ratios $^{176}Hf/^{177}Hf$ = 0.28325 and $^{176}Lu/^{177}Hf$ = 0.0384 [62]; [d] Two-stage model age (T_{DM2}) was calculated by projecting the initial $^{176}Hf/^{177}Hf$ ratios of the zircon back to the depleted mantle model growth curve, assuming a $^{176}Lu/^{177}Hf$ value of 0.015 for the average continent crust [63].

6.4. Whole-Rock Major and Trace Element Analyses

The major- and trace-element compositions of the SAFG are shown in Table 4 as weight percent (wt %) for major oxides and as parts per million (ppm) for all trace elements. According to the QAP ternary diagram [64] (Figure 8a), all samples classify as alkali-feldspar granite. They are characterized by high SiO_2 (74.89–76.83 wt %), Al_2O_3 (12.34–12.85 wt %) and alkali earths ($Na_2O + K_2O$ = 8.17–8.81 wt %) with low MgO (0.09–0.16 wt %) and CaO (0.08–0.24 wt %). They exhibit a high-K calc-alkaline, peraluminous and high-silica content, with A/CNK (molar $Al_2O_3/CaO + Na_2O + K_2O$) ranging from 1.04 to 1.12 and A/NK (molar $Al_2O_3/Na_2O + K_2O$) from 1.06 to 1.14 (Figure 8b,c). The inner phase has slightly higher SiO_2 content with lower Fe_2O_3, TiO_2, CaO and P_2O_5 than the outer phase (Table 4). This may indicate that SAFG cooled from the margin into the centre and that this cooling process resulted in a slightly more evolved inner phase. Both phases exhibit enriched REEs (except Eu) with total REE ranging from 147 ppm to 357 ppm. They are characterized by slightly enriched light REE (LREE, $(La/Yb)_N$ = 2.02–6.57) and flat heavy REE (HREE, $(Gd/Yb)_N$ = 0.6–1.27) with strong negative Eu anomalies (δEu = 0.05–0.12, Figure 9b). All samples are enriched in large-ion lithophile elements (LILEs, e.g., Rb, Th, U and K), high-field-strength elements (HFSEs, e.g., Nb, Ta, Zr and Hf), and exhibit strong depletion of Ba, Sr, P and Ti (Figure 9a).

Table 4. Major oxides and trace elements of the Shanshenfu alkali-feldspar granite.

Sample	The Inner Phase			The Outer Phase		
	SF-1	**SF-2**	**SF-3**	**SF-4**	**SF-5**	**SF-6**
SiO_2	76.83	75.23	76.02	76.22	74.89	75.36
Al_2O_3	12.34	12.56	12.78	12.67	12.85	12.54
Fe_2O_3	1.51	1.48	1.37	1.64	2.13	1.95
CaO	0.08	0.11	0.09	0.19	0.21	0.24
MgO	0.14	0.12	0.11	0.16	0.09	0.12
Na_2O	3.71	4.08	3.87	3.67	4.23	4.13
K_2O	4.46	4.31	4.42	4.87	4.53	4.68
TiO_2	0.15	0.27	0.19	0.17	0.25	0.31
MnO	0.06	0.08	0.04	0.11	0.05	0.06
P_2O_5	0.03	0.08	0.04	0.06	0.11	0.08
LOI	0.45	0.67	0.54	0.24	0.48	0.37
Total	99.98	99.56	99.71	100.32	99.67	99.48
La	52.3	22.6	45.5	58.8	27.2	40.1
Ce	161	54.2	101.3	174.5	72.3	89.6
Pr	14.75	6.58	13.2	15.1	7.22	12.6
Nd	53.6	20.8	44.2	51.3	29.1	45.5
Sm	12.8	5.13	9.35	11.26	7.32	9.81
Eu	0.34	0.15	0.13	0.42	0.17	0.21
Gd	10.72	5.82	7.62	10.11	9.61	6.97
Tb	1.91	1.28	1.18	1.83	2.36	1.11
Dy	12.3	10.44	7.61	12.28	13.12	6.5
Ho	2.54	2.35	1.51	2.57	2.68	1.27
Er	8.57	7.42	4.83	7.93	6.68	5.24
Tm	1.25	1.11	0.68	1.17	0.97	0.72
Yb	8.65	8.03	4.97	8.21	7.32	5.16
Lu	1.4	1.28	0.83	1.32	1.15	0.88
Ga	21.2	19.7	22.6	24.3	21.8	18.9
Rb	177	153.5	172	181.5	167	148
Ba	60.2	107	171	58.6	123	86
Th	16.3	17.51	14.2	17.1	18.2	13.6
U	3.79	3.65	3.48	2.87	3.67	3.13
Ta	2.23	2.65	2.31	2.95	2.46	2.33
Nb	43.7	49.1	44.3	48.2	46.2	44.7
Sr	8.3	14.8	22.4	24.1	15.3	18.7
Zr	358	435	647	248	487	276
Hf	11.9	13.1	18.4	10.8	13.9	11.2
Y	70.4	75.1	81.8	54.2	78.3	63.1
ΣREE	342	147	243	357	187	226
ΔEu	0.09	0.08	0.05	0.12	0.06	0.08

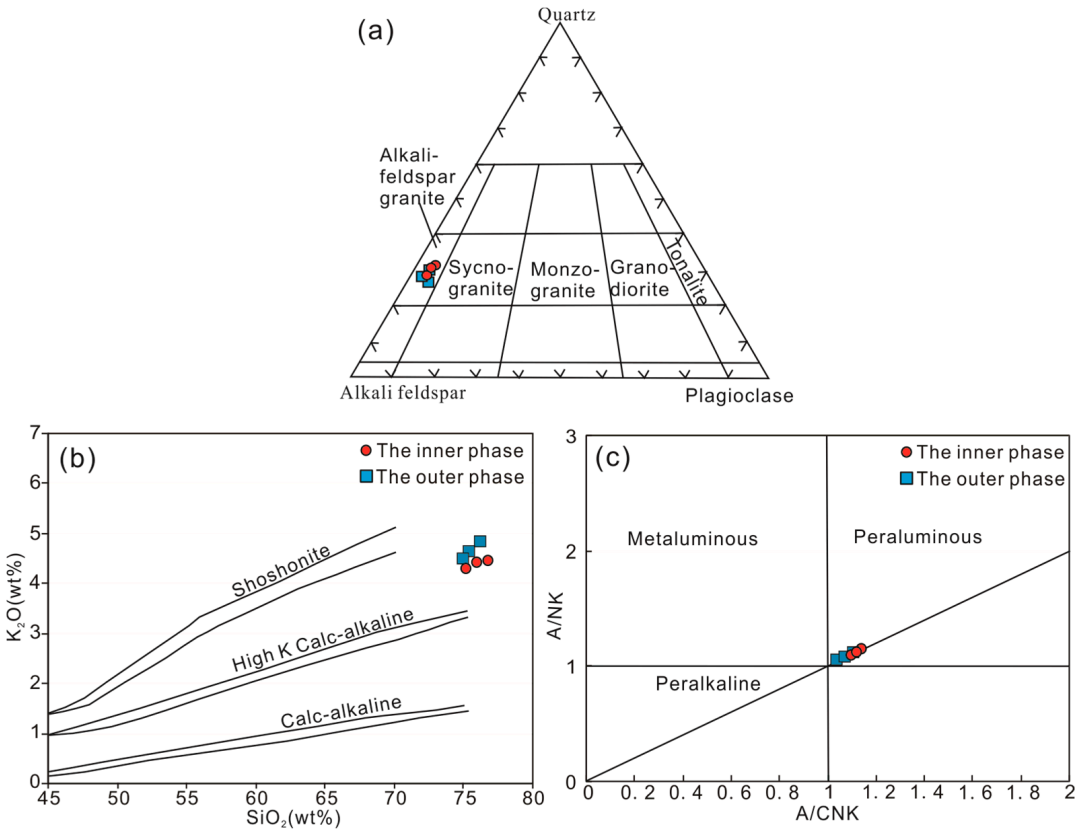

Figure 8. (**a**) QAP ternary diagram [64]; (**b**) SiO_2 vs. K_2O diagram of the Shanshenfu alkali-feldspar granite [65]; (**c**) A/NK vs. A/CNK diagram, where A/NK = $Al_2O_3/(Na_2O + K_2O)$ and A/CNK = $Al_2O_3/(CaO + Na_2O + K_2O)$ (all oxides on molar basis).

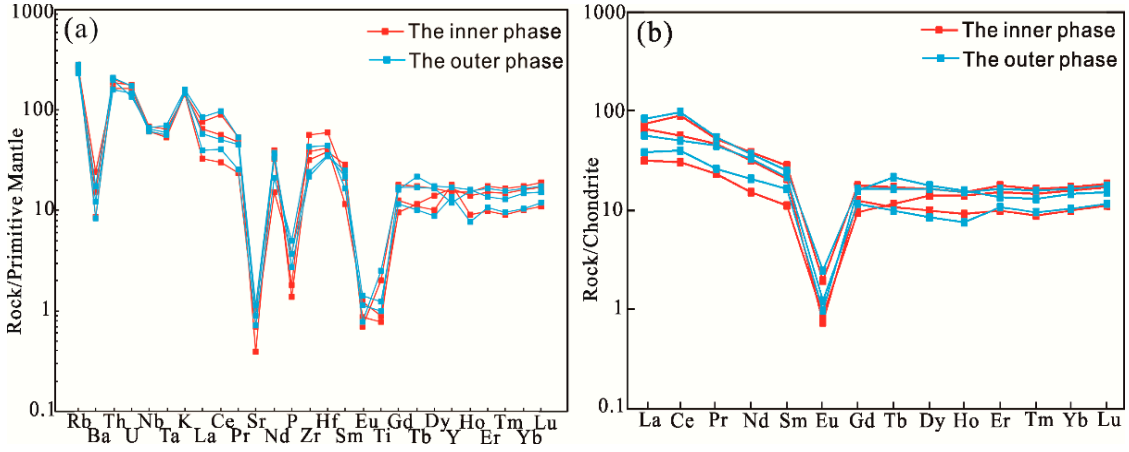

Figure 9. (**a**) Primitive mantle-normalized trace element diagram; (**b**) chondrite-normalized REE pattern. Normalization values are from Sun and McDonough [66].

7. Discussion

7.1. Genetic Type and Magmatic Oxygen Fugacity

The SAFG has high SiO_2 (74.89–76.83 wt %), total alkalis (K_2O + Na_2O = 8.17–8.81 wt %) and low P_2O_5 (0.03–0.11 wt %) contents (Table 4). It is enriched in HFSE (e.g., Nb, Ta, Zr and Hf) and REEs (except Eu), and is depleted in Sr, Ba, P, Ti and Eu (Figure 8c). These geochemical features are common for A-type granites [4]. An A-type granite classification is also supported by the elevated Ga content of all samples such that they plot in the A-type field on the discrimination diagram of Whalen et al. [67] (Figure 10a) and the within-plate-granite field on the diagram Y vs. Nb of Pearce et al. [68] (Figure 10b). Chondrite normalized REE patterns of zircons show they are depleted in LREE and enriched in HREE, and exhibit strong positive Ce anomalies (δCe = 1.22–275.99) and deep negative Eu anomalies (δEu = 0.1–0.38, Figure 7), which are typical of unaltered magmatic zircons [19]. Positive Ce anomalies may be related to a relatively oxidized melt with favorable incorporation of Ce^{4+} while negative Eu anomalies may be resulted from plagioclase fractionation in magma composition [17,18]. Due to the close relationship between the Ce anomaly in zircon and the oxidation state of the melt from which the zircon crystallizes [17,18], zircon can indicate the fo_2 of magmas. By plotting the Ti-in-zircon temperatures and the logarithmic oxygen fugacities on T vs. lg(fo_2) diagram (Figure 10c) that can be divided by the curves of some specific mineral oxidation buffers such as magnetite-hematite (MH), fayalite-magnetite-quartz (FMQ) and iron-wustite (IW) into several oxygen fugacity fields [17], nearly two thirds of the data points plot above the FMQ buffer (Figure 10c), which indicates oxidized magmatic conditions. The presence of magnetite (Figure 4d) and absence of significant amounts of ilmenite also suggest the oxidized magmatic conditions for the SAFG [12].

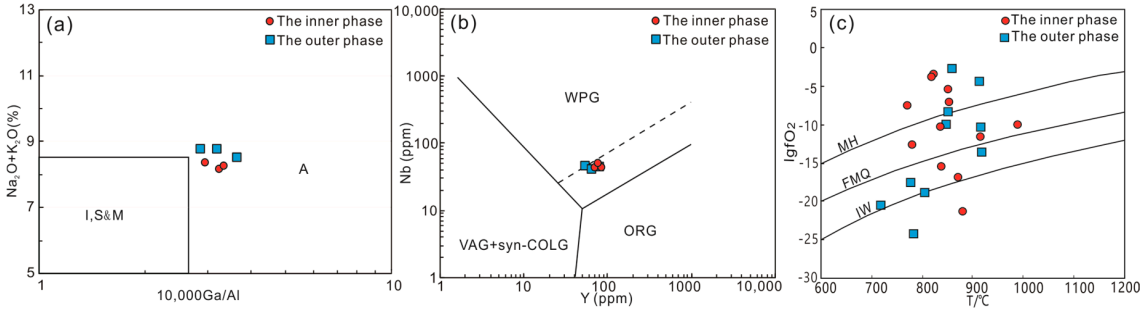

Figure 10. (**a**) K_2O + Na_2O vs. 10,000 Ga/Al discrimination diagram of Whalen et al. [67]. I, S and M—I-, S- and M-type granites; (**b**) Y vs. Nb tectonic discrimination diagram of Pearce et al. [68]. VAG—volcanic arc granites, WPG—within plate granites, COLG—collisional granites, ORG—oceanic ridge granites; (**c**) magmatic oxygen fugacity (fo_2) of the Shanshenfu alkali-feldspar granite, MH, FMQ and IW curves are from Trail et al. [17].

7.2. Petrogenesis and Implications for Mineralization

Several petrogenetic models have been proposed for the origin of A-type granites, including (1) extreme fractional crystallization of mantle-derived tholeiitic or alkaline basaltic magmas [6,69]; (2) low-degree partial melting of lower-crustal granulites with depletion of incompatible elements [70]; (3) anatexis of underplated I-type tonalitic crustal source [12,71,72]; and (4) hybridization between anatectic crustal and mantle-derived magmas, such as crustal assimilation and fractional crystallization of mantle-derived magmas, or of mixing between mantle-derived and crustal magmas [72–74]. The zircons of the SAFG exhibit high $\varepsilon_{Hf}(t)$ values (from +6.0 to +9.9) and young T_{DM2} (394–614 Ma, Table 3), which is consistent with juvenile crustal sources. Thus, we can rule out the possibility of partial melting of lower-crustal granulites, which would have a more isotopically evolved signature. The Ti-in-zircon temperatures of the SAFG are between 721–990 °C, which suggests that anatexis of underplated I-type tonalitic crust is unlikely to be the source because that process cannot provide the required high

temperature needed for the formation of A-type granites [6,75]. In addition, this magma source is not compatible with the observed elemental variations (e.g., Nb, Ta, Ti, P, Sr and Eu) in the SAFG [66]. Due to the absence of spatially or temporally associated alkaline mafic rocks in the study area [76], alkaline basaltic juvenile crust is not a suitable source for the SAFG. Thus, Two petrogenetic models that may explain the characteristics reported here for the SAFG are discussed further: (1) Extreme fractional crystallization from mantle-derived tholeiitic magma, and (2) hybridization between anatectic crustal and mantle-derived magmas.

Numerous studies suggest that the high magmatic oxygen fugacity is closely related to the nature of magma source regions [30,77,78]. The SAFG not only has similar U-Pb age and $\varepsilon_{Hf}(t)$ values to late Carboniferous arc intrusions from northern inner Mongolia (Figure 11a,b), but also has the high oxygen fugacity similar to arc magmas that can range from FMQ to FMQ + 6 [77]. The chemistry of zircon is related to the magma from which the zircon crystallized, two recent discrimination diagrams proposed by Grimes et al. [22] suggest zircon with relatively higher U or lower Yb or Y are sourced from continental crust, whereas zircon with lower U or higher Yb or Y are sourced from ocean crust. In Figure 11c,d, most of the studied zircons plot in the field of ocean crust zircon or in the intersection between continental zircon and ocean crust zircon. The evidence above suggest that arc-related juvenile crust is a possible source for the SAFG. This magma source of Permian A-type granites in the CAOB has been proposed by previous studies [76,79]. The depletion of Nb, Ta, Ti, P, Sr and Eu in the SAFG indicates contamination and metasomatism by subducting oceanic crust [80]. This is also consistent with peraluminous nature and muscovite reported in mineralogy. Therefore, we propose that the SAFG was derived from the crustal assimilation and fractional crystallization of juvenile crust metasomatized by subducting oceanic crust. This magma source is similar to charnockitized juvenile crust proposed by previous studies [79,81–83].

Based on related studies conducted on Cu-Au-Mo hydrothermal deposits, the link between oxidized felsic magmas and mineralization is well recognized [13,27,73,78,84]. Sun et al. [27,78] documented that sulfur in melt exists mainly as SO and SO_2 at high fo_2 and as S^{2-} at low fo_2. Numerous experiments suggested that the partition coefficients of chalcophile elements (e.g., Cu, Au and Mo) between silicate melt and pyrrhotite are positively correlated with fo_2 [84–86]. Therefore, high fo_2 of the SAFG favors transmission of the chalcophile elements (e.g., Cu and Au) of the source region into the melt together with oxidized sulfur, rather than into the sulfides (reduced sulfur) [17,25,26,38,78,87]. With the decrease of temperature and pressure, hydrous magma can release a water-rich volatile phase to form a magmatic-hydrothermal ore-forming system [88]. Mao et al. [89] revealed the magmatic-hydrothermal mineralization process of the SAFG in detail through the study of melt-fluid inclusions. In this process metals such as Cu can be effectively enriched in the fluid phases after magmatic fractional crystallization due to high fo_2 and high exsolution temperature of the SAFG [89], consequently facilitating subsequent Cu-polymetallic hydrothermal mineralization.

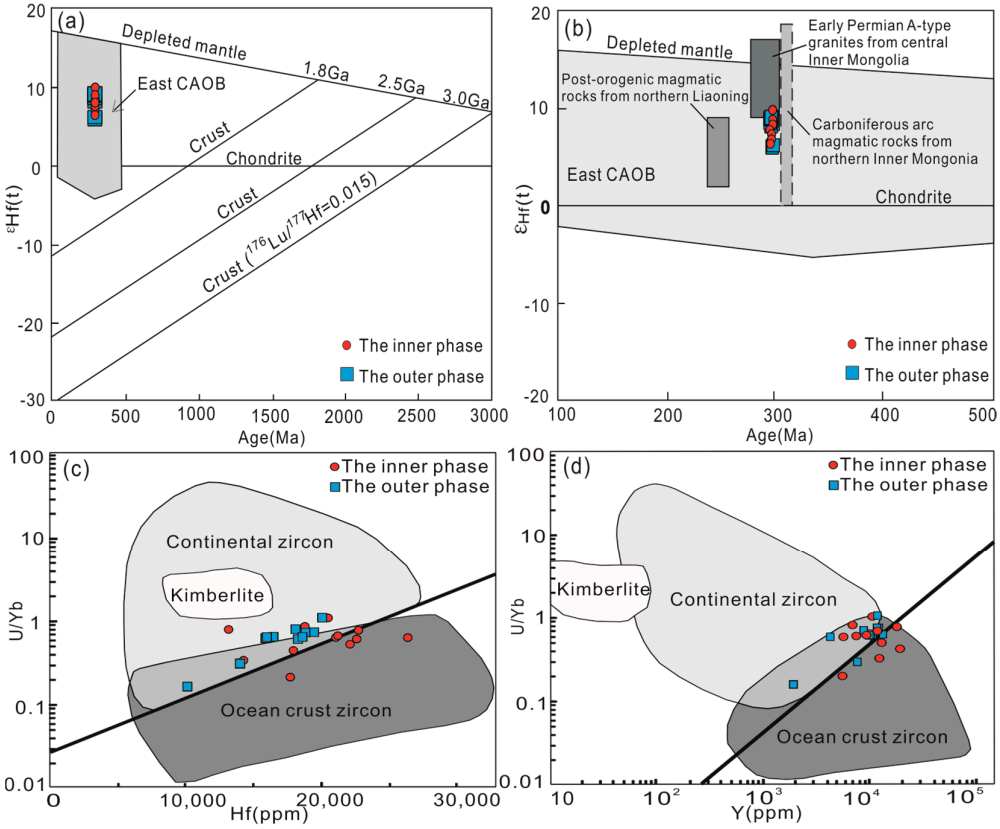

Figure 11. (**a**,**b**) Compilation diagram of ε_{Hf} (t) vs. U-Pb age of the Shanshenfu alkali-feldspar granite. The Hf isotopic evolution line of the Archean average crust with $^{176}Lu/^{177}Hf$ = 0.015 is after Griffin et al. [62]. The fields for Carboniferous arc intrusions from northern inner Mongolia, early Permian A-type granites from central inner Mongolia and late Permian to early Triassic post-orogenic melts from northern Liaoning are from Chen et al. [36], Zhang et al. [79] and Zhang et al. [90], respectively. (**c**,**d**) U/Yb ratio vs. Y and Hf content diagrams of Grimes et al. [22] to discriminate between continental and oceanic crust zircon. Heavy lines indicate the lower limit of zircons from continental crust.

7.3. Extensional Setting for Cu-Polymetallic Mineralization

Recent studies suggest that Cu-polymetallic mineralization associated with extensional setting in the XMOB was mainly formed in the early Cretaceous [10,91–93]. The extensional setting for Cu-polymetallic mineralization in the Permian is rarely reported. Therefore, the clear tectonic setting of the Permian A-type granites associated with Cu-polymetallic mineralization along the HHSZ is of great significance for regional tectonic evolution and prospecting. The SAFG with an age of 298 Ma is not only contemporary with immense alkali granites from southern Mongolia [94], but also coincident with the equivalents in the central inner Mongolia [79] and Erguna-Xing'an terrane of NE China [4,34]. Eby [2] divided the A-type granites into A1 and A2 groups. The A1 group is emplaced in anorogenic settings such as plumes, hotspots or continental rift zones. The A2 group is related to a cycle of subduction-zone or continent-continent collision magmatism in crust and emplaced in a variety of tectonic settings. In our study, the SAFG plots in the A2 field on the Nb-Y-3Ga diagram of Eby [2] (Figure 12a), and plot in the post-collisional setting on the Y + Nb versus Rb plot of Pearce et al. [68] (Figure 12b). Such an environment is also supported by the previous studies for other Permian A-type granitoids along the HHSZ [4,78,95]. The SAFG together with the other Permian A2-type granites [3,4,29–31] are commonly found with Carboniferous calc-alkaline I-type plutons along the HHSZ [36]. The increase in granitoid alkalinity with time indicates the tectonic transition from an earlier arc setting to a later extensional setting [96]. Similar tendency also occurs in southern Mongolia [94,95] and central inner Mongolia [79].

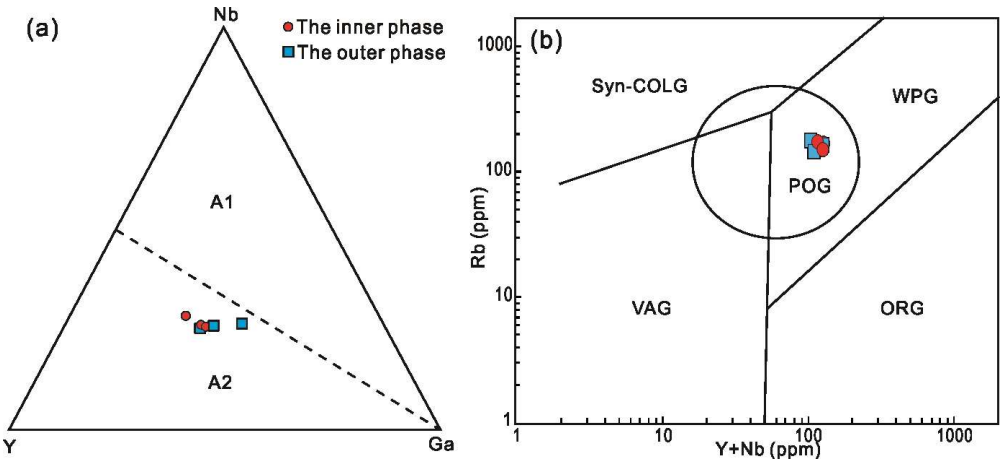

Figure 12. (**a**) Nb-Y-Ga ternary diagram of Eby [2]; (**b**) Y + Nb vs. Rb plot of Pearce et al. [68].

Previous studies suggest that the ocean along the Hegenshan-Heihe was closed during the late Carboniferous, which could be proved by the following evidences: (1) The Hegenshan ophiolite was emplaced before the early Permian, most likely between 300 Ma and 335 Ma [97,98]; (2) Permian and Carboniferous submarine turbidite strata with predominant magmatic arc source exists along the HHSZ [99]. However, the last Paleo-Asian ocean was not closed along the HHSZ during the late Carboniferous but closed along the Solonker-Xra Moron-Changchun suture during the late Permian–early Triassic [100]. This is well evidenced by late Permian to early Triassic post-orogenic magmatic rocks form belts along the Solonker-Xra Moron-Changchun suture [73,75]. Taking into account the fact that the Permian A2-type granites (260–300 Ma) are strikingly sparse and small in volume, and show a NE-trending migration together with the widespread occurrence of Permian volcanic rocks of island arc affinity and late Permian terrestrial sediments along the HHSZ [4], the post-collisional slab break-off process along the HHSZ during the Permian was generally proposed by previous studies [74,101]. Such tectonic regime is also evidenced by contemporaneous thermal metamorphism recorded by the Xilinhot metamorphic complexes in northern inner Mongolia [36], which once represented a segment of fore-arc basin [36]. In addition, the corresponding change can be observed in sedimentary style and clastic provenance of the early Permian strata from central inner Mongolia [102] and southern Mongolia [103]. The hallmark features of post-collisional slab break-off event is well recorded in numerous Phanerozoic cases [72,101,104], including transition in magmatic affinity from I-type to A-type, a narrow linear zone of magmatism, thermal metamorphismand change in uplift rate and concomitant sedimentary style [105]. All these features fit relatively well with the corresponding expressions along the HHSZ during Permian [4,36,102,103]. This unusual tectonic regime not only terminates a prolonged northward subduction of the Paleo-Asian ocean, but also heralds the amalgamation between the Songliao terrane and the Liaoyuan terrane along the Ondor Temple-Xar Moron suture zone.

The age of ore-related A-type granite in the Hongyan Cu-polymetallic deposit is consistent with the mineralized A-type granites in the southwestern part of the HHSZ [32], which suggests that these A-type granites associated with mineralization are formed in the same extension setting. During the Permian, the HHSZ was characterized by post-collisional extensional tectonism with the slab break-off, which not only caused upwelling of asthenospheric mantle and resulted in partial melting of the overlying lithospheric mantle and the juvenile arc crust [79], but also provided the thermal flux to form some narrow extensional magmatic channels, subsequently followed by A-type magmatism and related mineralization deposition along the HHSZ. Thus, the Permian A-type granites with arc-related juvenile crustal source and high fo_2 along the HHSZ have great potential for prospecting Cu-polymetallic hydrothermal deposits, and deserve more attention in future exploration.

8. Conclusions

Based upon geochronological and geochemical data from the SAFG, we suggest the following:

(1) LA-ICP-MS U-Pb zircon dating shows the inner phase and outer phase of the SAFG were formed at 298.8 ± 1.0 Ma and 298.5 ± 1.0 Ma, respectively. This makes the SAFG an early Permian pluton.

(2) The SAFG is a typical A-type granite with high magmatic oxygen fugacity. The source for the SAFG magma includes both crustal assimilation and fractional crystallization of juvenile crust metasomatized by subducting oceanic crust.

(3) The oxidized magmatic conditions favor transport and enrichment of chalcophile elements (e.g., Cu and Au) while the arc-related juvenile source favors Cu and Au enrichment. Combined, these magmatic characteristics suggest related magmatic-hydrothermal mineralization may be restricted to Cu ± Au.

(4) Combined with regional geological background, the Permian A-type granites and related mineralization along the HHSZ were formed in post-collisional extensional tectonism with the slab break-off.

Author Contributions: Data curation, C.M.; Formal analysis, C.M.; Funding acquisition, X.L.; Investigation, C.M., X.L. and C.C.; Project administration, X.L. and C.C.; Writing—original draft, C.M.; Writing—review & editing, C.M., X.L. and C.C.

Funding: This research was supported by the Geological Survey Project of China Geological Survey Bureau (NMKD2010-3).

Acknowledgments: We gratefully thank Ruan Banxiao and Yang Yongsheng from Institute of Geological Survey, China University of Geosciences, Wuhan, for their important guidance and assistance in geochemical analysis.

Conflicts of Interest: The authors declare no conflict of interest.

References

1. Loiselle, M.C.; Wones, D.R. Characteristics and origin of anorogenic granites. *Geol. Soc. Am. Abstr. Prog.* **1979**, *11*, 468.
2. Eby, G.N. Chemical subdivision of the A-type granitoids: Petrogenetic and tectonic implications. *Geology* **1992**, *20*, 641–644. [CrossRef]
3. Hong, D.W.; Huang, H.Z.; Xiao, Y.J.; Xu, H.M. Permian alkaline granites in center Inner Mongolia and their geodynamic significance. *Acta Geol. Sin.* **1994**, *68*, 219–230. (In Chinese) [CrossRef]
4. Wu, F.Y.; Sun, D.Y.; Li, H.M.; Jahn, B.M.; Wilde, S. A-type granites in northeastern China: Age and geochemical constraints on their petrogenesis. *Chem. Geol.* **2002**, *187*, 143–173. [CrossRef]
5. Wu, S.P.; Wang, M.Y.; Qi, K.J. Present situation of researches on A-type granites: A review. *Acta Petrol. Mineral.* **2007**, *26*, 57–66, (In Chinese with English Abstract). [CrossRef]
6. Bonin, B. A-type granites and related rocks: Evolution of a concept, problems and prospects. *Lithos* **2007**, *97*, 1–29. [CrossRef]
7. Li, H.; Watanabe, K.; Yonezu, K. Geochemistry of A-type granites in the Huangshaping polymetallic deposit (South Hunan, China): Implications for granite evolution and associated mineralization. *J. Asian Earth Sci.* **2014**, *88*, 149–167. [CrossRef]
8. Li, H.; Palinkaš, L.A.; Watanabe, K.; Xi, X.S. Petrogenesis of Jurassic A-type granites associated with Cu-Mo and W-Sn deposits in the central Nanling region, South China: Relation to mantle upwelling and intra-continental extension. *Ore Geol. Rev.* **2018**, *92*, 449–462. [CrossRef]
9. Liu, P.; Mao, J.W.; Santosh, M.; Bao, Z.A.; Zeng, X.Z.; Jia, L.H. Geochronology and petrogenesis of the Early Cretaceous A-type granite from the Feie'shan W-Sn deposit in the eastern Guangdong Province, SE China: Implications for W-Sn mineralization and geodynamic setting. *Lithos* **2018**, *300*, 330–347. [CrossRef]
10. Wang, X.D.; Xu, D.M.; Lv, X.B.; Wei, W.; Mei, W.; Fan, X.J.; Sun, B.K. Origin of the Haobugao skarn Fe-Zn polymetallic deposit, Southern Great Xing'an range, NE China: Geochronological, geochemical, and Sr-Nd-Pb isotopic constraints. *Ore Geol. Rev.* **2018**, *94*, 58–72. [CrossRef]

11. Cisse, M.; Lü, X.B.; Algeo, T.J.; Cao, X.F.; Li, H.; Wei, M.; Yuan, Q.; Chen, M. Geochronology and geochemical characteristics of the Dongping ore-bearing granite, North China: Sources and implications for its tectonic setting. *Ore Geol. Rev.* **2017**, *89*, 1091–1106. [CrossRef]
12. Dall'Agnol, R.; Oliveira, D.C. Oxidized, magnetite-series, rapakivi-type granites of Carajás, Brazil: Implications for classification and petrogenesis of A-type granites. *Lithos* **2007**, *93*, 215–233. [CrossRef]
13. Qiu, J.T.; Yu, X.Q.; Santosh, M.; Zhang, D.H.; Chen, S.Q.; Li, J.P. Geochronology and magmatic oxygen fugacity of the Tongcun molybdenum deposit, northwest Zhejiang, SE China. *Miner. Depos.* **2013**, *48*, 545–556. [CrossRef]
14. Frost, C.D.; Frost, B.R. Reduced rapakivi-type granites: The tholeiite connection. *Geology* **1997**, *25*, 647–650. [CrossRef]
15. Watson, E.B.; Wark, D.A.; Thomas, J.B. Crystallization thermometers for zircon and rutile. *Contrib. Mineral. Petrol.* **2006**, *151*, 413–433. [CrossRef]
16. Ferry, J.M.; Waston, E.B. New thermodynamic models and revised calibrations for the Ti-in-zircon and Zr-in-rutile thermometers. *Contrib. Mineral. Petrol.* **2007**, *154*, 429–437. [CrossRef]
17. Trail, D.; Watson, E.B.; Tailby, N.D. The oxidation state of Hadean magmas and implications for early Earth's atmosphere. *Nature* **2011**, *480*, 79–82. [CrossRef]
18. Trail, D.; Watson, E.B.; Tailby, N.D. Ce and Eu anomales in zircon as proxies for oxidation state of magmas. *Geochim. Cosmochim. Acta* **2012**, *97*, 70–87. [CrossRef]
19. Hoskin, P.W.O.; Schaltegger, U. The composition of zircon and igneous and metamorphic petrogenesis. *Rev. Mineral. Geochem.* **2003**, *53*, 27–62. [CrossRef]
20. Hanchar, J.M.; VanWestrenen, W. Rare earth element behavior in zircon-melt systems. *Elements* **2007**, *3*, 37–42. [CrossRef]
21. Hoskin, P.W.O. Trace-element composition of hydrothermal zircon and the alteration of Hadean zircon from the Jack Hills, Australia. *Geochim. Cosmochim. Acta* **2005**, *69*, 637–648. [CrossRef]
22. Grimes, C.B.; John, B.E.; Kelemen, P.B.; Mazdab, F.K.; Wooden, J.L.; Cheadle, M.J.; Hanghøj, K.; Schwartz, J.J. Trace element chemistry of zircons from oceanic crust: A method for distinguishing detrital zircon provenance. *Geology* **2007**, *35*, 643–646. [CrossRef]
23. Yang, J.H.; Wu, F.Y.; Wilde, S.A.; Xie, L.W.; Yang, Y.H.; Liu, X.M. Tracing magma mixing in granite genesis: In situ U–Pb dating and Hf-isotope analysis of zircons. *Contrib. Mineral. Petrol.* **2007**, *153*, 177–190. [CrossRef]
24. Cherniak, D.J.; Watson, E.B. Diffusion in zircon. *Rev. Mineral. Geochem.* **2003**, *53*, 113–143. [CrossRef]
25. Maughan, D.T.; Keith, J.D.; Christiansen, E.H.; Pulsipher, T.; Hattori, K.; Evans, N.J. Contributions from mafic alkaline magmas to the Bingham porphyry Cu-Au-Mo deposit, Utah, USA. *Miner. Depos.* **2002**, *37*, 14–37. [CrossRef]
26. Ma, X.H.; Chen, B.; Yang, M.C. Magma mixing origin for the Aolunhua porphyry related to Mo-Cu mineralization, eastern Central Asian Orogenic belt. *Gondwana Res.* **2013**, *24*, 1152–1171. [CrossRef]
27. Sun, W.D.; Liang, H.Y.; Ling, M.X.; Zhan, M.Z.; Ding, X.; Zhang, H.; Yang, X.Y.; Li, Y.L.; Ireland, T.R.; Wei, Q.R.; et al. The link between reduced porphyry copper deposits and oxidized magmas. *Geochim. Cosmochim. Acta* **2013**, *103*, 263–275. [CrossRef]
28. Lu, Y.J.; Loucks, R.R.; Fiorentini, M.L.; McCuaig, T.C.; Evans, N.J.; Yang, Z.M.; Hou, Z.Q.; Kirkland, C.L.; Parra-Avila, L.A.; Kobussen, A. Zircon compositions as a pathfinder for porphyry Cu ± Mo ± Au deposits. *Soc. Econ. Geol. Spec. Publ.* **2016**, *19*, 329–347.
29. Shi, G.H.; Miao, L.C.; Zhang, F.Q.; Jian, P.; Fan, W.M.; Liu, D.Y. The age and its district tectonic implications on the Xilinhaote A-type granites, Inner Mongolia. *Chin. Sci. Bull.* **2004**, *49*, 384–389. (In Chinese) [CrossRef]
30. Zhang, Y.Q.; Xu, L.Q.; Kang, X.L. Age dating of alkali granite in Jingesitai area of Dong Ujingqin Banner, Inner Mongolia, and its significance. *Geol. Chin.* **2009**, *36*, 988–995. (In Chinese) [CrossRef]
31. Guo, K.C.; Zhang, W.L.; Yang, X.P.; Wang, L.; Shi, D.Y.; Yu, H.T.; Su, H. Origin of early Permian A-type granite in the Wudaogou area, Heihe City. *J. Jilin Univ. (Earth Sci. Ed.)* **2011**, *41*, 1077–1083, (In Chinese with English abstract). [CrossRef]
32. Yang, K. Ore-forming Characters and Depositing Orientation of Metal Deposit in the Dong Ujimqin, Inner Mongolia. Master's Thesis, China University of Geosciences in Wuhan, Wuhan, China, 2013.
33. Mao, J.W.; Pirajno, F.; Cook, N. Mesozoic metallogeny in East China and corresponding geodynamic settings—An introduction to the special issue. *Ore Geol. Rev.* **2011**, *43*, 1–7. [CrossRef]

34. Wu, F.Y.; Sun, D.Y.; Ge, W.C.; Zhang, Y.B.; Grant, M.L.; Wilde, S.A.; Jahn, B.M. Geochronology of the Phanerozoic granitoids in northeastern China. *J. Asian Earth Sci.* **2011**, *41*, 1–30. [CrossRef]
35. Gao, S.; Xu, H.; Zang, Y.; Wang, T. Mineralogy, ore-forming fluids and geochronology of the Shangmachang and Beidagou gold deposits, Heilongjiang province, NE China. *J. Geochem. Explor.* **2018**, *188*, 137–155. [CrossRef]
36. Chen, B.; Jahn, B.M.; Tian, W. Evolution of the Solonker suture zone: Constraints from zircon U-Pb ages, Hf isotopic ratios and whole-rock Nd–Sr isotope compositions of subduction and collision-related magmas and forearc sediments. *J. Asian Earth Sci.* **2009**, *34*, 245–257. [CrossRef]
37. Zhang, X.H.; Xue, F.H.; Yuan, L.L.; Wilde, S.A. Late Permian appinite–granite complex from northwestern Liaoning, North China craton: Petrogenesis and tectonic implications. *Lithos* **2012**, *155*, 201–217. [CrossRef]
38. Wang, Y.H.; Zhao, C.B.; Zhang, F.F.; Liu, J.J.; Wang, J.P.; Peng, R.M.; Liu, B. SIMS zircon U-Pb and molybdenite Re-Os geochronology, Hf isotope, and whole-rock geochemistry of the Wunugetushan porphyry Cu-Mo deposit and granitoids in NE China and their geological significance. *Gondwana Res.* **2015**, *28*, 1228–1245. [CrossRef]
39. Zhou, Z.H.; Mao, J.W.; Wu, X.L.; Ouyang, H.G. Geochronology and geochemistry constraints of the Early Cretaceous Taibudai porphyry Cu deposit, northeast China, and its tectonic significance. *J. Asian Earth Sci.* **2015**, *103*, 212–228. [CrossRef]
40. Wei, R.H.; Gao, Y.F.; Xu, S.C.; Xin, H.T.; Santosh, M.; Liu, Y.F.; Lei, S.H. The volcanic succession of Baoligaomiao, central Inner Mongolia: Evidence for Carboniferous continental arc in the central Asian orogenic belt. *Gondwana Res.* **2017**, *51*, 234–254. [CrossRef]
41. Wu, G.; Chen, Y.C.; Sun, F.Y.; Liu, J.; Wang, G.R.; Xu, B. Geochronology, geochemistry, and Sr–Nd–Hf isotopes of the early Paleozoic igneous rocks in the Duobaoshan area, NE China, and their geological significance. *J. Asian Earth Sci.* **2015**, *97*, 229–250. [CrossRef]
42. Liu, W.; Liu, X.J.; Liu, L.Q. Underplating generated A- and I-type granitoids of the East Junggar from the lower and the upper oceanic crust with mixing of mafic magma: Insights from integrated zircon U-Pb ages, pertrography, geochemistry and Nd-Sr-Hf isotopes. *Lithos* **2013**, *179*, 293–319. [CrossRef]
43. Mao, J.W.; Wang, Y.T.; Zhang, Z.H.; Yu, J.J.; Niu, B.G. Geodynamic settings of Mesozoic large-scale mineralization in North China adjacent areas. *Sci. Chin. Ser. D* **2003**, *46*, 838–851. [CrossRef]
44. Zhang, F.F.; Wang, Y.H.; Liu, J.J.; Wang, J.P.; Zhao, C.B.; Song, Z.W. Origin of the Wunugetushan porphyry Cu–Mo deposit, Inner Mongolia, NE China: Constraints from geology, geochronology, geochemistry, and isotopic compositions. *J. Asian Earth Sci.* **2016**, *117*, 208–224. [CrossRef]
45. Zeng, Q.D.; Liu, J.M.; Zhang, L.C. Re-Os geochronology of porphyry molybdenum deposit in southern segment of Da Hinggan Mountains, Northeast China. *J. Earth Sci.* **2010**, *21*, 390–401. [CrossRef]
46. Yang, Y.S. Metallogenic Specialization of Gold, Copper and Molybdenum Mineralized Igneous Rocks in Middle-Northern Great Xing'an Range and Metallogenic Prediction in Hongyan Area. Ph.D. Thesis, China University of Geosciences in Wuhan, Wuhan, China, 2017.
47. Hassan, M.H.; Reinhard, K.; Tomoyuki, S. Genetically related Mo-Bi-Ag and U-F mineralization in A-type granite, Gabal Gattar, Eastern Desert, Egypt. *Ore Geol. Rev.* **2014**, *62*, 181–190. [CrossRef]
48. Bunyamin, A. Geochemical associations between fluorite mineralization and A-type shoshonitic magmatism in the Keban-Elazig area, East Anatolia, Turkey. *J. Afr. Earth Sci.* **2015**, *11*, 222–230. [CrossRef]
49. Liu, Y.S.; Hu, Z.C.; Gao, S.; Günther, D.; Xu, J.; Gao, C.G.; Chen, H.H. In situ analysis of major and trace elements of anhydrous minerals by LA-ICP-MS without applying at internal standard. *Chem. Geol.* **2008**, *257*, 34–43. [CrossRef]
50. Liu, Y.S.; Gao, S.; Hu, Z.C.; Gao, C.G.; Zong, K.Q.; Wang, D.B. Continental and oceanic crust recycling-induced melt-peridotite interactions in the Trans-North China Orogen: U-Pb dating, Hf isotopes and trace elements in zircons of mantle xenoliths. *J. Petrol.* **2010**, *51*, 537–571. [CrossRef]
51. Ludwig, K.R. Isoplot 3.00. A Geochronological toolkit for microsoft excel. *Berkeley Geochronol. Center Spec. Publ.* **2003**, *3*, 1–70.
52. Qiu, J.T.; Song, W.J.; Jiang, C.X.; Wu, H.; Dong, R.M. CGDK: An extensible CorelDRAW VBA program for geological drafting. *Comput. Geosci.* **2013**, *51*, 34–48. [CrossRef]

53. Hu, Z.C.; Liu, Y.S.; Gao, S.; Liu, W.G.; Yang, L.; Zhang, W.; Tong, X.R.; Lin, L.; Zong, K.Q.; Li, M. Improved in situ Hf isotope ratio analysis of zircon using newly designed X skimmer cone and Jet sample cone in combination with the addition of nitrogen by laser ablation multiple collector ICP-MS. *J. Anal. At. Spectrom.* **2012**, *27*, 1391–1399. [CrossRef]
54. Woodhead, J.; Herget, J.; Shelley, M.; Eggins, S.; Kemp, R. Zircon Hf-isotope analysis with an excimer laser, depth profiling, ablation of complex geometries, and concomitant age estimation. *Chem. Geol.* **2004**, *209*, 121–135. [CrossRef]
55. Wu, F.Y.; Yang, Y.H.; Xie, L.W.; Yang, J.H.; Xu, P. Hf isotopic compositions of the standard zircons and baddeleyites used in U-Pb geochronology. *Chem. Geol.* **2006**, *234*, 105–126. [CrossRef]
56. Li, X.H.; Li, Z.X.; Wingate, M.T.D.; Chung, S.L.; Liu, Y.; Lin, G.C.; Li, W.X. Geochemistry of the 755 Ma Mundine Well dyke swarm, northwestern Australia: Part of a Neoproterozoic mantle superplume beneath Rodinia? *Precambr. Res.* **2006**, *146*, 1–15. [CrossRef]
57. Hiess, J.; Nutman, A.P.; Bennett, V.C.; Holden, P. Ti-in-zircon thermometry applied to contrasting Archean metamorphic and igneous systems. *Chem. Geol.* **2008**, *247*, 323–338. [CrossRef]
58. McDonough, W.F.; Sun, S.S. The composition of the Earth. *Chem. Geol.* **1995**, *120*, 223–253. [CrossRef]
59. Myers, J.; Eugster, H.P. The system Fe-Si-O: Oxygen buffer calibrations to 1500 K. *Contrib. Mineral. Petrol.* **1983**, *82*, 75–90. [CrossRef]
60. Soderlund, U.; Patchett, P.J.; Vervoort, J.D.; Isachsen, C.E. The ^{176}Lu decay constant determined by Lu-Hf and U-Pb isotope systematic of Precambrian mafic intrusions. *Earth Planet. Sci. Lett.* **2004**, *219*, 311–324. [CrossRef]
61. Blichert-Toft, J.; Chauvel, C.; Albarede, F. Separation of Hf and Lu for high-precision isotope analysis of rock samples by magnetic sector-multiple collector ICP-MS. *Contrib. Mineral. Petrol.* **1997**, *127*, 248–260. [CrossRef]
62. Griffin, W.L.; Pearson, N.J.; Belousova, E.; Jackson, S.E.; Achterbergh, E.V.; O'Reilly, S.Y.; Shee, S.R. The Hf isotope composition of cratonicmantle: LAM-MC-ICPMS analysis of zircon megacrysts in kimberlites. *Geochim. Cosmochim. Acta* **2000**, *64*, 133–147. [CrossRef]
63. Griffin, W.L.; Wang, X.; Jackson, S.E.; Pearson, N.J.; O'Reilly, S.Y.; Xu, X.; Zhou, X. Zircons chemistry and magma genesis in SE China: In situ analysis of Hf isotopes, Pingtan and Tonglu igneous complexes. *Lithos* **2002**, *61*, 237–269. [CrossRef]
64. Strecheissen, A. To each plutonic rock its proper name. *Earth Sci. Rev.* **1976**, *12*, 1–33. [CrossRef]
65. Peccerillo, A.; Taylor, S.R. Geochemistry of Eocen calc-alkaline volcanic rocks from the Kastamounu area, northern Turkey. *Contrib. Miner. Petrol.* **1976**, *58*, 63–81. [CrossRef]
66. Sun, S.S.; McDonough, W.F. Chemical and isotopic systematics of oceanic basalts: Implications for mantle composition and processes. *Geol. Soc. Lond. Spec. Publ.* **1989**, *42*, 313–345. [CrossRef]
67. Whalen, J.B.; Currie, K.L.; Chappell, B.W. A-type granites: Geochemical characteristics, discrimination and petrogenesis. *Contrib. Mineral. Petrol.* **1987**, *95*, 407–419. [CrossRef]
68. Pearce, J.A.; Harris, N.B.W.; Tindle, A.G. Trace-element discrimination diagrams for the tectonic interpretation of granitic-rocks. *J. Petrol.* **1984**, *25*, 956–983. [CrossRef]
69. Patino Douce, A.E. What do experiments tell us about the relative contributions of crust and mantle to the origin of granitic magmas? *Geol. Soc. Lond. Spec. Publ.* **1999**, *168*, 55–75. [CrossRef]
70. Huang, H.Q.; Li, X.H.; Li, W.X.; Li, Z.X. Formation of high δ^{18}O fayalite-bearing A-type granite by high-temperature melting of granulitic metasedimentary rocks, southern China. *Geology* **2011**, *39*, 903–906. [CrossRef]
71. Patino Douce, A.E. Generation of metaluminous A-type granites by low-pressure melting of calc-alkaline granitoids. *Geology* **1997**, *25*, 743–746. [CrossRef]
72. Dall'Agnol, R.; Frost, C.D.; Ramo, O.T. IGCP Project 510 "A-type granites and related rocks through time": Project vita, results, and contribution to granite research. *Lithos* **2012**, *151*, 1–16. [CrossRef]
73. Han, Y.G.; Zhang, S.H.; Pirajno, F.; Zhou, X.W.; Zhao, G.C.; Qu, W.J.; Liu, S.H.; Zhang, J.M.; Liang, H.B.; Yang, K. U-Pb and Re-Os isotopic systematics and zircon Ce^{4+}/Ce^{3+} ratios in the Shiyaogou Mo deposit in eastern Qinling, central China: Insights into the oxidation state of granitoids and Mo (Au) mineralization. *Ore Geol. Rev.* **2013**, *55*, 29–47. [CrossRef]

74. Zhang, X.H.; Yuan, L.L.; Xue, F.H.; Zhang, Y. Contrasting Triassic ferroan granitoids from northwestern Liaoning, North China: Magmatic monitor of Mesozoic decratonization and craton–orogen boundary. *Lithos* **2012**, *144*, 12–23. [CrossRef]
75. Touret, J.L.R. Fluid inclusions and pressure-temperature estimates in deep-seated rocks. In *Chemical Transport in Metasomatic Processes*; Helgeson, H.C., Ed.; NATO ASI Series: Brussels, Belgium, 1987; Volume 218, pp. 91–121.
76. Wei, R.H.; Gao, Y.F.; Xu, S.C.; Santosh, M.; Xin, H.T.; Zhang, Z.M.; Li, W.L.; Liu, Y.F. Carboniferous continental arc in the Hegenshan accretionary belt: Constrains from plutonic complex in central Inner Mongolia. *Lithos* **2018**, *308*, 242–261. [CrossRef]
77. Lee, C.T.A.; Leeman, W.P.; Canil, D.; Canil, D.; Li, Z.X.A. Similar V/Sc systematics MORB and arc basalts: Implications for the oxygen fugacities of their mantle source regions. *J. Petrol.* **2005**, *46*, 2313–2336. [CrossRef]
78. Sun, W.D.; Huang, R.F.; Li, H.; Hu, Y.B.; Zhang, C.C.; Sun, S.J.; Zhang, L.P.; Ding, X.; Li, C.Y.; Zartman, R.E. Porphyry deposits and oxidized magmas. *Ore Geol. Rev.* **2015**, *65*, 97–131. [CrossRef]
79. Zhang, X.H.; Yuan, L.L.; Xue, F.H.; Yan, X.; Mao, Q. Early Permian A-type granites from central Inner Mongolia, North China: Magmatic tracer of post-collisional tectonics and oceanic crustal recycling. *Gondwana Res.* **2015**, *28*, 311–327. [CrossRef]
80. Fitton, J.G.; James, D.; Lccman, W.P. Basic magmatism associated with the late Cenozoic extension in the western United States: Compositional variations in space and time. *Geophys. Res.* **1991**, *13*, 693–711. [CrossRef]
81. Yuan, L.; Zhang, X.; Xue, F.; Liu, F. Juvenile crustal recycling in an accretionary orogen: Insights from contrasting early permian granites from central Inner Mongolia, North China. *Lithos* **2016**, *264*, 524–539. [CrossRef]
82. Landenberger, B.; Collins, W.J. Derivation of A-type granites from a dehydrated charnockitic lower crust: Evidence from the Chaelundi Complex, Eastern Australia. *J. Petrol.* **1996**, *37*, 145–170. [CrossRef]
83. Zhao, X.F.; Zhou, M.F.; Li, J.W.; Wu, F.Y. Association of neoproterozoic A-and I-type granites in South China: Implications for generation of A-type granites in a subduction-related environment. *Chem. Geol.* **2008**, *257*, 1–15. [CrossRef]
84. Mengason, M.J.; Candela, P.A.; Piccoli, P.M. Molybdenum, tungsten and manganese partitioning in the system pyrrhotite–Fe–S–O melt–rhyolite melt: Impact of sulfide segregation on arc magma evolution. *Geochim. Cosmochim. Acta* **2011**, *75*, 7018–7030. [CrossRef]
85. Jugo, P.; Candela, P.; Piccoli, P. Magmatic sulfides and Au: Cu ratios in porphyry deposits: An experimental study of copper and gold partitioning at 850 °C, 100 MPa in a haplogranitic melt–pyrrhotite–intermediate solidsolution–gold metal assemblage, at gas saturation. *Lithos* **1999**, *46*, 573–589. [CrossRef]
86. Yang, X.M.; Lentz, D.R.; Sylvester, P.J. Gold contents of sulfide minerals in granitoids from southwestern New Brunswick, Canada. *Miner. Depos.* **2006**, *41*, 369–386. [CrossRef]
87. Thompson, J.F.H.; Sillitoe, R.H.; Baker, T.; Lang, J.R.; Mortensen, J. Intrusion-related gold deposits associated with tungsten-tin provinces. *Miner. Depos.* **1999**, *34*, 323–334. [CrossRef]
88. Burnham, C.W. Magmas and hydrothermal fluids. In *Geochemistry of Hydrothermal Ore Deposits*, 3rd ed.; Barnes, H.L., Ed.; JohnWiley and Sons: New York, NY, USA, 1997; pp. 63–123.
89. Mao, C.; Lu, X.B.; Chen, C.; Cao, M.Y.; Gun, M.S.; Liao, P.C.; Jia, Q.Y. Melt-fluid inclusions study of Shanshenfu granite and its mineralization significance in Hongyan Town, Inner Mongolia. *Earth Sci.* **2016**, *41*, 139–152, (In Chinese with English Abstract).
90. Zhang, J.H.; Gao, S.; Ge, W.C.; Wu, F.Y.; Yang, J.H.; Wilde, S.A.; Li, M. Geochronology of the mesozoic volcanic rocks in the Great Xing'an Range, northeastern China: Implications for subduction-induced delamination. *Chem. Geol.* **2010**, *276*, 144–165. [CrossRef]
91. Mei, W.; Lv, X.B.; Liu, Z.; Tang, R.K.; Ai, Z.L.; Wang, X.D.; Cisse, M. Geochronological and geochemical constraints on the ore-related granites in Huanggang deposit, Southern Great Xing'an Range, NE China and its tectonic significance. *Geosci. J.* **2015**, *19*, 53–67. [CrossRef]
92. Zhai, D.G.; Liu, J.J.; Zhang, H.Y.; Yao, M.J.; Wang, J.P.; Yang, Y.Q. S-Pb isotopic geochemistry, U-Pb and Re-Os geochronology of the Huangganggliang Fe–Sn deposit, Inner Mongolia, NE China. *Ore Geol. Rev.* **2014**, *59*, 109–122. [CrossRef]

93. Ruan, B.X.; Lv, X.B.; Yang, W.; Liu, S.T.; Yu, Y.M.; Wu, C.M.; Munir, M.A.A. Geology, geochemistry and fluid inclusions of the Bianjiadayuan Pb-Zn-Ag deposit, Inner Monglia, NE China: Implications for tectonic setting and metallogeny. *Ore Geol. Rev.* **2015**, *71*, 121–137. [CrossRef]
94. Blight, J.H.S.; Crowley, Q.G.; Petterson, M.G.; Cunningham, D. Granites of the southern Mongolia Carboniferous arc: New geochronological and geochemical constraints. *Lithos* **2010**, *116*, 35–52. [CrossRef]
95. Blight, J.H.S.; Petterson, M.G.; Crowley, Q.G.; Cunningham, D. The Oyut Ulaan volcanic group: Stratigraphy, magmatic evolution and timing of Carboniferous arc development in SE Mongolia. *J. Geol. Soc. Lond.* **2010**, *167*, 491–509. [CrossRef]
96. Litvinovsky, B.A.; Tsygankov, A.A.; Jahn, B.M.; Katzir, Y.; Be'eri-Shlevin, Y. Origin and evolution of overlapping calc-alkaline and alkalinemagmas: The late palaeozoic post-collisional igneous province of transbaikalia (Russia). *Lithos* **2011**, *125*, 845–874. [CrossRef]
97. Zhou, J.B.; Han, J.; Zhao, G.C.; Zhang, X.Z.; Cao, J.L.; Pei, S.H.; Wang, B. The emplacement time of the Hegenshan Ophiolite: Constraints from the unconformably overlying paleozoic strata. *Tectonophysics* **2015**, *622*, 398–415. [CrossRef]
98. Pei, S.H.; Zhou, J.B.; Li, L. U–Pb ages of detrital zircon of the Paleozoic sedimentary rocks: New constraints on the emplacement time of the Hegenshan ophiolite, NE China. *J. Asian Earth Sci.* **2016**, *130*, 75–87. [CrossRef]
99. Eizenhöfer, P.R.; Zhao, G.; Sun, M.; Zhang, J.; Han, Y.G.; Hou, W. Geochronological and Hf isotopic variability of detrital zircons in Paleozoic strata across the accretionary collision zone between the North China craton and Mongolian arcs and tectonic implications. *Geol. Soc. Am. Bull.* **2015**, *127*, 1422–1436. [CrossRef]
100. Han, J.; Zhou, J.B.; Wang, B.; Cao, J.L. The final collision of the CAOB: Constraint from the zircon U–Pb dating of the Linxi Formation, Inner Mongolia. *Geosci. Front.* **2015**, *6*, 211–225. [CrossRef]
101. Janasi, V.; Vlach, S.R.F.; Campos Neto, M.; Ulbrich, H.H.G.J. Associated A-type subalkaline and high-K calc-alkaline granites in the Itu granite province, southeastern Brazil: Petrological and tectonic significance. *Can. Mineral.* **2009**, *47*, 1505–1526. [CrossRef]
102. Li, D.P.; Chen, Y.L.; Wang, Z.; Hou, K.; Liu, C.Z. Detrital zircon U–Pb ages, Hf isotopes and tectonic implications for Palaeozoic sedimentary rocks from the Xing-Meng Orogenic Belt, Middle-East part of Inner Mongolia, China. *Geol. J.* **2011**, *46*, 63–81. [CrossRef]
103. Lamb, M.A.; Badarch, G. Paleozoic sedimentary basins and volcanic arc systems of southern Mongolia; new geochemical and petrographic constraints. *Geol. Soc. Am. Mem.* **2001**, *194*, 117–149.
104. Whalen, J.B.; McNicoll, V.J.; van Staal, C.R.; Lissenberg, C.J.; Longstaffe, F.J.; Jenner, G.A.; van Breeman, O. Spatial, temporal and geochemical characteristics of Silurian collision-zone magmatism, Newfoundland Appalachians: An example of a rapidly evolving magmatic system related to slab break-off. *Lithos* **2006**, *89*, 377–404. [CrossRef]
105. Bonin, B. Do coeval mafic and felsic magmas in post-collisional to within-plate regimes necessarily imply two contrasting, mantle and crustal, sources? A review. *Lithos* **2004**, *78*, 1–24. [CrossRef]